Late Paleozoic and Mesozoic Magmatism in Jilin Area, NE China: Implications for the Transition from Convergence at the Paleo-Asian Ocean to Paleo-Pacific Subduction

Jin–Peng Luan[1,2], Wen–Liang Xu[1,3*], Gideon Rosenbaum[2], Jack F. Ward[2], Peng Guo[1], Jian-Guo Wang[1]

[1]College of Earth Sciences, Jilin University, Changchun 130061, China

[2]School of Earth and Environmental Sciences, The University of Queensland, Brisbane, Queensland 4072, Australia

[3]Key Laboratory of Mineral Resources Evaluation in Northeast Asia, Ministry of Land and Resources, Changchun 130061, China

Corresponding author: Wen-Liang Xu (xuwl@jlu.edu.cn)

Key Points:

- P_2 to J_2 magmatism is identified in Jilin area in the eastern Central Asian Orogenic Belt
- Final closure of the Paleo-Asian Ocean occurred at 244–227 Ma, and its double subduction resulted in P_2 to T_1 magmatism
- Tectonic regime transition from the convergence of Paleo-Asian Ocean to subduction of Paleo-Pacific Ocean occurred at T_3 to J_1

Abstract

During the late Paleozoic and Mesozoic, convergent plate boundary processes in northeastern Asia shifted from the Paleo-Asian Ocean to Paleo-Pacific Ocean, influencing the tectonic regime. To better understand this tectonic transition, we investigated the petrology, geochronology and geochemistry of igneous rocks from the Jilin area in the eastern part of the Central Asian Orogenic Belt. We identified four stages of magmatism at ~261, 253–244, 183–175 and 173–164 Ma. The ~261 Ma magmatism was generated in an active continental margin by partial melting of juvenile mafic lower crustal material. This stage of continental arc magmatism continued with the emplacement of 253–244 Ma adakitic magamas, which were generated by partial melting of subducted oceanic crustal material and metasomatized with overlying mantle wedge. The 183–175 Ma monzogranitic and dioritic magmas were generated in a continental arc environment via melting of juvenile lower continental crust and mixing of basaltic magma with crustal melt, respectively. Magmatism at 173–164 Ma was developed in an active continental margin, and were generated by melting of a juvenile lower continental crust. The integrated evidence suggests that the closure of the Paleo-Asian Ocean could occur at 244–227 Ma, whereas the timing of tectonic regime transition from the convergence of Paleo-Asian Ocean to the subduction of the Paleo-Pacific Ocean occurred at 223–185 Ma. The Changchun-Yanji Suture, which marks the easternmost closure of the Paleo-Asian Ocean, experienced multiple tectonic mode switches, and was controlled by subduction of the Paleo-Pacific Ocean since Early Jurassic.

1 Introduction

The eastern part of the Central Asian Orogenic Belt (CAOB) occupies the area between the Siberian and North China cratons, and consists of microcontinental massifs, accretionary orogens and other terranes (Fig. 1; Sengör et al., 1993; Ye and Zhang, 1994; Jahn, 2000; Xie, 2000; Xiao et al., 2003, 2015; Li et al., 2006). The microcontinental massifs in the eastern CAOB, which include the Erguna, Xing'an, Songnen, Jiamusi, and Khanka massifs, consist of Archean to Neoproterozoic continental crust (Khanchuk et al., 2010; Wu et sl., 2011; Tang et al., 2013; Zhao et al., 2016; Han et al., 2017; Luan et al., 2017a, b, 2019; Yang et al., 2017, 2018; Qian et al., 2018; Zhang et al., 2018; Xu et al., 2019). Separating these massifs are the faults and/or accretionary orogens, and the architecture of the region is dominated by the Mongol-Okhotsk Orogen, South Mongolian-Great Khing'an Orogen, and Suolunshan-Central Jilin Orogen (Fig. 1; Li et al., 2006). They were produces of subduction of the Paleo-Asian Ocean, and were affected by subsequent evolution of the Mongol-Okhotsk Ocean and the Paleo-Pacific Ocean.

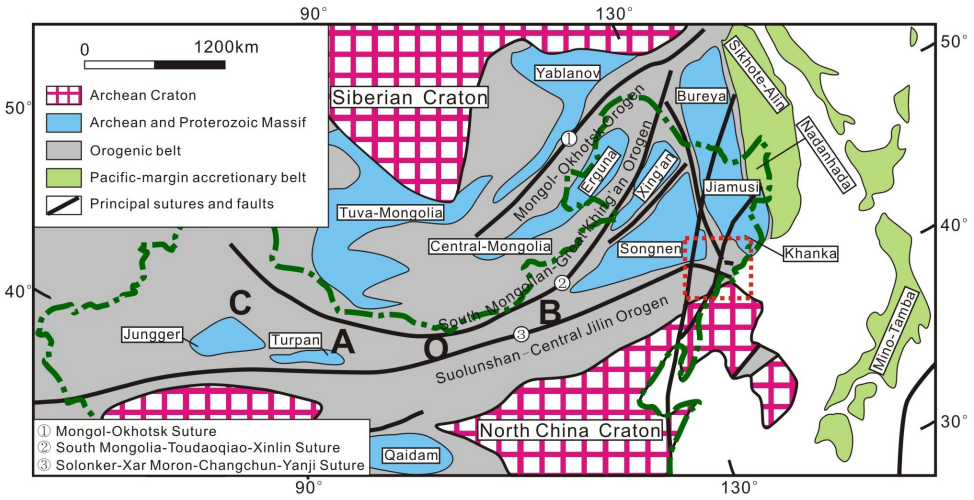

Figure 1. Simplified tectonic map of the northeastern Asian continent (after Li et al., 2006).

During the Paleozoic and early Mesozoic, the tectonic evolution of northeastern China and adjacent regions was closely linked to plate tectonic processes along the margins of the Paleo-Asian and Paleo-Pacific oceans (Li, 2006; Xu et al., 2009, 2013; Wu et al., 2011; Liu et al., 2017; Wang et al., 2017, 2019; Zhou et al., 2017a, 2018). Subsequently, during the Mesozoic and Cenozoic, the tectonic regime was influenced mainly by processes along the Mongol-Okhotsk and western Pacific oceans (Li et al., 2015, 2020; Xu et al., 2009, 2013; Tang et al., 2016). The CAOB in northeastern China is a key area for understanding the transition from the earlier influence of the Paleo-Asian Ocean to the later influence of the Paleo-Pacific Ocean.

The Paleo-Asian Ocean was consumed entirely by subduction processes, with the suture marked by the Solonker Suture (Wu et al., 2002; Xiao et al., 2003; Li, 2006) and its eastward extension along the Xar Moron-Changchun (Wu et al., 2002) and Changchun-Yanji sutures (Li, 2006) (Fig. 1). However, the timing of ocean closure at the Paleo-Asian Ocean and the timing of subduction initiation at the Paleo-Pacific Ocean are a matter of debate. For the Paleo-Asian Ocean, the final closure has been suggested to occur in the late Permian to Early Triassic (Li et al., 2006; Cao et al., 2013; Eizenhöfer et al., 2014; Safonova and Santosh, 2014; Wang et al.,

2015; Ma et al., 2017, 2019), Middle to Late Triassic (Zhou et al., 2014; Shi et al., 2019; Wang et al., 2019), or Early–Middle Jurassic (Sun et al., 2004, 2005; Wu et al., 2007; Zhou et al., 2009; Yu et al., 2012). Better constraints on the timing of deformation and magmatism along the Solonker-Xar Moron-Changchun-Yanji Suture might help understanding the timing of this tectonic transition.

In this paper, we present new geochronological, whole-rock geochemical data, and zircon Hf isotopic data from middle Permian to Middle Jurassic igneous rocks that occur near the Changchun-Yanji Suture in the area of Jilin city (Fig. 2). Using these new data, we aim to: (1) constrain the timing of magmatism and elucidate the spatio-temporal distribution of magmatism; (2) characterize the petrogenesis of the igneous rocks and their possible sources; and (3) provide new insights into the tectonic setting during magmatism. The collective geological and geochemical data from this area allow us to better understand the transition in the tectonic regime during the Paleozoic and Mesozoic.

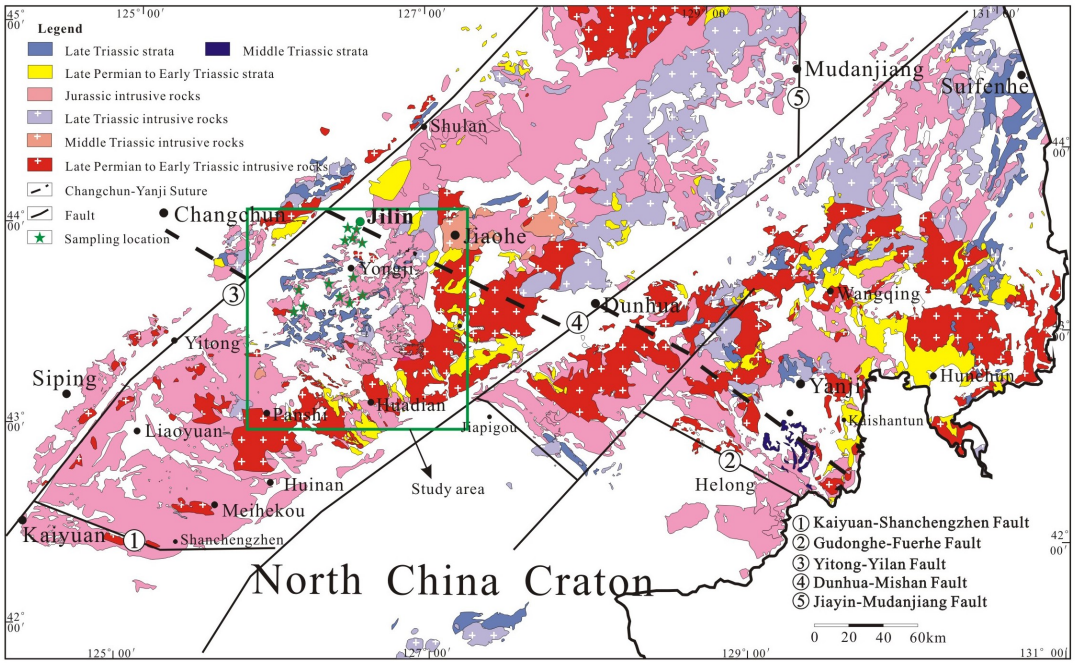

Figure 2. Detailed geological map of the eastern part of the Suolunshan-Central Jilin Orogen.

87 Table 1: Geochronological data for the intrusive rocks in central Jilin area

Order	Sample	GPS Location		Lithology	Model minerals (Vol %)								Age	References
		Longitude	Latitude		Q	Af	Pl	Bi	Hb	Cpx	SP	AM		
Late Permian														
1	17JZ9-1	126°01'57"	43°19'45"	Syenogranite	25	50	20				Mt 3%	2	261±1 Ma	This study
2	12JL1-1	126°01'10"	43°23'56"	Syenogranite	30	48	20					2	260±1 Ma	Cao et al., 2013
3	LK36-1	125°44'41"	42°52'12"	Syenogranite	45	30	18	5				2	259±2 Ma	Cao et al., 2013
4	17JZ4-1	126°31'36"	43°24'54"	Monzonite	5	30	30	2	25	5	Mt 4%	1	253±2 Ma	This study
5	13JH1-1	125°59'52"	43°26'42"	Quartz monzonite	15	35	40		8			2	252±2 Ma	Wang et al., 2015
6	DY143-2	125°06'22"	43°02'31"	Monzogranite									252±2 Ma	Wu et al., 2011
Early Triassic														
7	DY123-4	125°57'29"	43°06'40"	Alkali feldspar granite									251±2 Ma	Wu et al., 2011
8	9923-1	126°28'05"	43°07'55"	Granodiorite									248±4 Ma	Wu et al., 2011
9	42758	126°28'05"	43°07'55"	Granodiorite									248±4 Ma	Wu et al., 2011
10	YZ02-27-5	128°49'32"	43°03'10"	Monzogranite									248±2 Ma	Zhang et al., 2004
11	FW00-110	128°51'02"	43°07'33"	Monzogranite									247±1 Ma	Wu et al., 2011
12	12LY2-1	125°24'13"	43°02'42"	Monzogranite	32	32	30	4				2	247±1 Ma	Cao et al., 2013
Middle Triassic														
13	JK5-2	126°26'45"	43°11'02"	Hornblende gabbro									246±4 Ma	Wang et al., 2013
14	YZ02-22-2	128°49'21"	42°12'14"	Monzogranite									245±6 Ma	Zhang et al., 2004
15	YZ02-25-2	128°44'58"	42°10'57"	Monzogranite									245±3 Ma	Zhang et al., 2004
16	14YT14-1	125°17'16"	43°17'34"	Monzogranite	30	28	34				Ms 5%	2	244±2 Ma	Wang et al., 2015
17	17JZ5-1	126°29'54"	43°22'49"	Quartz monzonite	10	25	40	5	17			3	244±2 Ma	This study
Late Triassic														
18	FW00-50	128°33'13"	43°04'28"	Hornblende diorite									223±1 Ma	Wu et al., 2011
19	99SW109	126°25'22"	42°53'52"	Gabbro									216±5 Ma	Wu et al., 2004
20	FW00-73	130°57'58"	43°53'30"	Monzogranite									214±10 Ma	Wu et al., 2011
Early Jurassic														
21	9718-1	126°58'50"	43°50'54"	Alkali feldspar granite									190±2 Ma	Wu et al., 2002
22	FW00-56	129°06'19"	42°59'02"	Monzogranite									186±1 Ma	Wu et al., 2011
23	DY0506-1	126°31'46"	42°47'26"	Syenogranite									185±2 Ma	Wu et al., 2011
24	HTW1-1	129°12'51"	48°32'24"	Hornblende gabbro									185±2 Ma	Yu et al., 2012
25	9909-4	125°21'28"	42°57'15"	Monzogranite									184±3 Ma	Wu et al., 2011
26	D1-7	126°29'48"	43°58'24"	Monzogranite	30	24	40	3				3	181±1 Ma	This study
27	DY0504-2	126°27'20"	42°45'20"	Syenogranite									182±3 Ma	Wu et al., 2011
28	DY118-1	126°45'03"	43°05'06"	Granodiorite									182±2 Ma	Wu et al., 2011
29	FW00-54	126°59'28"	42°02'31"	Granodiorite									182±2 Ma	Wu et al., 2011
30	HYC10-1	128°23'23"	47°42'37"	Hornblende gabbro									182±2 Ma	Yu et al., 2012
31	DY0509-5	126°35'14"	42°59'18"	Diorite									182±1 Ma	Wu et al., 2011
32	17JZ1-1	126°27'55"	43°31'58	Monzogranite	26	35	32	5				2	181±1 Ma	This study
33	17JZ3-1	126°25'23"	43°25'37"	Monzogranite	30	25	40	4				1	181±1 Ma	This study
34	17JZ2-1	126°25'23"	43°25'37"	Monzogranite	25	30	35	5			Ms 3%	2	180±1 Ma	This study
35	17JZ6-1	126°18'44"	43°33'07"	Monzogranite	30	30	30	4	4			2	180±1 Ma	This study
36	DY020-1	125°17'12"	43°17'30"	monzogranite									178±4 Ma	Wu et al., 2011
37	DY023-2	125°16'40"	43°14'48"	Syenogranite									178±2 Ma	Wu et al., 2011
38	D5-1	126°28'08"	43°52'19"	Monzogranite	28	25	43	3				1	178±2 Ma	This study
39	DY018-1	126°10'30"	43°23'35"	Monzogranite									177±2 Ma	Wu et al., 2011
40	98SW126	126°55'01"	43°53'56"	Diorite inclusion									175±4 Ma	Wu et al., 2011
41	98SW125	126°55'01"	43°53'56"	Monzogranite									175±3 Ma	Wu et al., 2011
42	SCS01-1	126°08'30"	42°59'25"	Granodiorite									175±3 Ma	Wu et al., 2011
43	LK20-2	126°13'41"	43°21'10"	Monzogranite									175±2 Ma	Zhang et al., 2016
44	D6-1	126°27'50"	43°52'08"	Diorite	5	10	60	8	15			2	175±2 Ma	This study
45	D15-1	126°31'34"	43°50'21"	Monzogranite	25	23	45	5				2	175±2 Ma	This study
46	LK20-2	125°26'34"	43°23'05"	Monzogranite									175±1 Ma	Zhang et al., 2016

88

Continued Table 1

Order	Sample	GPS Location		Lithology	Model minerals (Vol %)								Age	References
		Longitude	Latitude		Q	Af	Pl	Bi	Hb	Cpx	SP	AM		
47	15JJW6	126°31'22"	43°16'08"	Granite									175±1 Ma	Zhang et al., 2016
Middle Jurassic														
48	SC02	126°45'28"	41°49'48"	Monzogranite									174±3 Ma	Sun et al., 2005
49	98SW124	126°43'44"	43°58'10"	Granodiorite									173±4 Ma	Wu et al., 2011
50	D1-1	126°29'48"	43°58'24"	Monzogranite	30	35	30	3				2	173±3 Ma	This study
51	FW00-88	126°31'52"	43°38'10"	Monzogranite									173±2 Ma	Wu et al., 2011
52	MG-12	125°12'14"	42°55'45"	Monzogranite									171±6 Ma	Wu et al., 2011
53	17JZ8-1	126°08'15"	43°22'52"	Monzogranite	30	28	35	5				2	171±2 Ma	This study
54	17JZ7-1	126°05'38"	43°28'15"	Syenogranite	30	50	15	4				1	171±1 Ma	This study
55	17JZ8-4	126°08'15"	43°22'52"	Monzogranite	30	30	35	3				2	171±1 Ma	This study
56	97103-1	126°19'50"	43°06'05"	Granodiorite									170±1 Ma	Wu et al., 2011
57	FW00-37	127°52'50"	42°47'49"	Monzogranite	25	18	40	15				2	168±3 Ma	Zhang et al., 2002
58	DY144-1	126°31'31"	43°51'16"	Syenogranite									166±2 Ma	Wu et al., 2011
59	D12-1	126°27'55"	42°56'32"	Monzogranite	32	25	35	5				3	164±5 Ma	This study
Late Jurassic														
60	DY141-1	125°07'58"	43°10'12"	Monzogranite									163±1 Ma	Wu et al., 2011
61	CH11	125°36'29"	43°37'47"	Monzogranite	40	30	27	2				1	162±2 Ma	Xu et al., 2008
62	SCS01-1	126°08'30"	42°59'25"	Granodiorite									161±3 Ma	Wu et al., 2011
63	X13	125°36'13"	43°36'05"	Syenogranite	30	58	10	1				1	159±3 Ma	Xu et al., 2008
64	DY129-5	124°48'11"	42°59'40"	Monzogranite									158±3 Ma	Wu et al., 2011
65	DY015-1	124°36'57"	42°36'03"	Monzogranite									158±4 Ma	Wu et al., 2011

Q:quartz; Af: alkali feldspar; Pl: plagioclase; Bi: biotite; Hb: hornblende; Cpx: clinopyroxene; Ms: muscovite; Mt: magnetite; SP:special mineral; AM:accessory mineral

2 Geological setting

The study area is located near the city of Jilin (Fig. 2). This area comprises the eastern part of the Suolunshan-Central Jilin Orogen, which is bounded by the Changchun-Yanji Suture in the north and the Kaiyuan-Shanchengzhen-Fuerhe Fault in the south (Fig. 2). These major structures are cut by two northeast-striking sinistral strike-slip faults (Fig. 2).

Widespread late Paleozoic to early Mesozoic igneous rocks occur in the eastern part of the Suolunshan-Central Jilin Orogen. Their ages can be subdivided into three groups: middle Permian to Middle Triassic (261–240 Ma), Late Triassic (223–214 Ma), and Early-Middle Jurassic (194–172 Ma). Middle Permian to Middle Triassic igneous rocks include mafic to felsic volcanic (trachyandesite and rhyolite) and intrusive (alkali granite, quartz diorite, granodiorite, and monzogranite) rocks, which are aligned along an E–W trending belt (Fig. 2; Wu et al., 2011; Yang et al., 2012; Xu et al., 2013; Ma et al., 2017, 2019). Late Triassic igneous rocks are

scattered in the study area, and consist of hornblende gabbro, trachyandesite, hornblende diorite, granodiorite, and monzogranite (Wu et al., 2011; Wang et al., 2019). Early Jurassic igneous rocks are I- and A-type granitoids, including granodiorite, monzogranite, syenogranite, and alkali-feldspar granite (Wu et al., 2011, Yu et al., 2013).

Sedimentary rocks in the study area are Carboniferous to Early Cretaceous in age (Jilin Bureau of Geology and Mineral Resources, JBGMR, 1988). Carboniferous rocks are dominated by marine volcano-sedimentary strata. Along the Changchun-Yanji Suture, ophiolitic material occurs in association with the late Carboniferous strata (Zheng et al., 1999，Zhou et al., 2009). Permian marine volcano-sedimentary strata are widespread in the study area. The Triassic strata are dominated by marine volcano-sedimentary rocks (Peng et al., 2012 and references therein), but the sedimentary environment gradually changes into terrestrial facies in the Late Triassic rocks. The Permian and Triassic strata are intruded by Permo–Triassic mafic to felsic plutons (Li, 2006; Wu et al., 2011; Zhou et al., 2017b). Jurassic and Cretaceous rocks are associated mainly with terrigenous clastic strata that contain abundant fossils. The deposition of these rocks was accompanied by volcanic activity (Xu et al., 2013).

3 Sampling and analytical methods

Samples of intrusive rocks were taken from 12 plutons in the area of Jilin city (Fig. 2). A summary of the petrography is summarized in Table 1. Representative photomicrographs are shown in Figure 3. Zircon U-Pb dating and Hf isotope analyses were performed at the Wuhan SampleSolution Analytical Technology Co., Ltd., whereas the whole-rock geochemical analyses were measured at the State Key Laboratory of Geological Processes and Mineral Resources of China University of Geosciences.

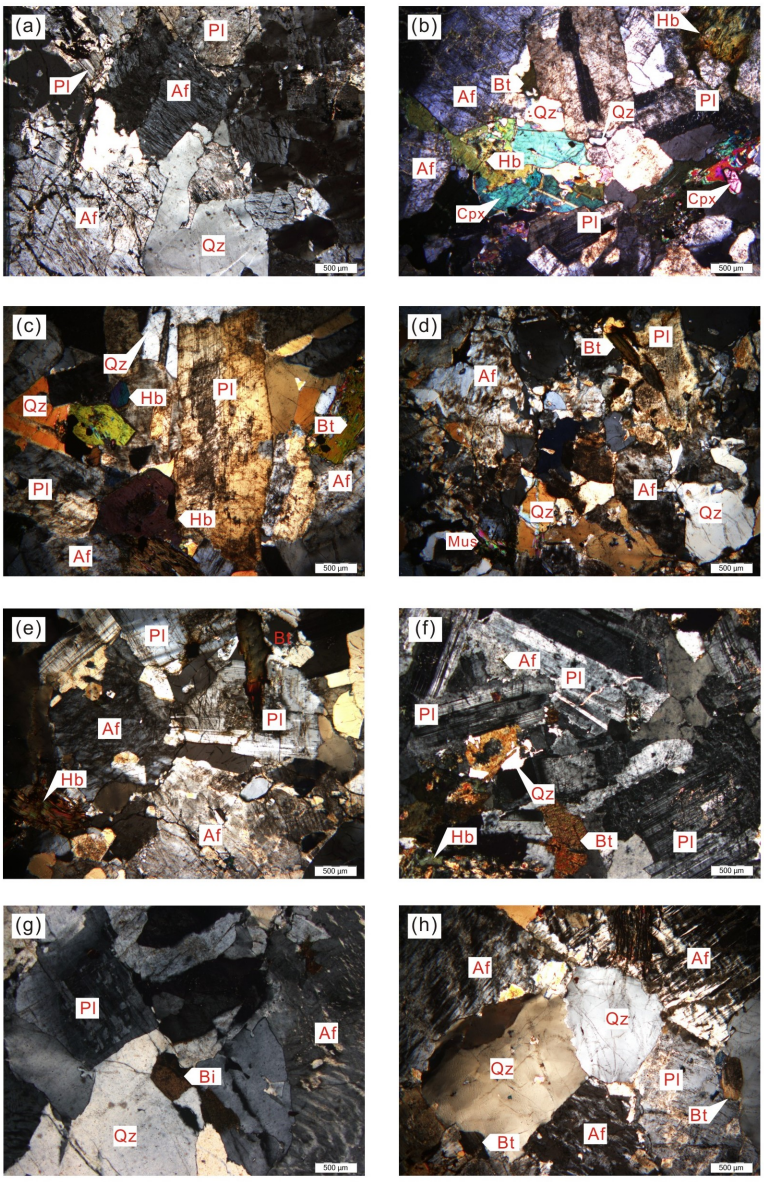

Figure 3. Photomicrographs (all cross-polarized light) of selected samples from the middle Permian to Middle Jurassic intrusive rocks in study area. Qz, quartz; Pl, plagioclase; Af, alkaline feldspar; Bt, biotite; Mus, muscovite; Hb, hornblende; Cpx, clinopyroxene.

3.1. Zircon U–Pb dating

Zircon grains were extracted from samples using standard density and magnetic separation techniques, followed by handpicking under a binocular microscope. Cathodoluminescence (CL) images were obtained to reveal internal structures of zircon. zircon U–Pb analyses were performed using an Agilent 7500a ICP–MS equipped with a 193 nm laser. The analyses created

a crater diameter of 32 μm. For further information on the instrument settings and analytical procedures, see Yuan et al. (2004). Data reduction and Correction for common Pb referred to methods by Liu et al. (2010), Ludwig (2003) and Anderson (2002). Results are presented in Table S1 in supplementary material.

3.2. Major and trace element analyses

Fresh samples were crushed into ~200 μm mesh size by using agate mill. Whole-rock sampled were then digested in Teflonbombs and measured for major and trace elements compositions using X–ray fluorescence (Rigaku RIX 2100 spectrometer), fused-glass disks and ICP–MS (Agilent 7500a with a shield torch). Analytical uncertainties are in the range of 1%–3%. The analytical results for the BHVO–1 (basalt), BCR–2 (basalt), and AGV–1 (andesite) standards indicate that the analytical precision is better than 5% and 10% for the major and trace elements, respectively (Rudnick et al., 2004). Results are presented in Table S2 in supplementary material.

3.3. Zircon Hf isotope analyses

In situ zircon Hf isotope analyses were performed using a Neptune MC–ICP–MS with an ArFexcimer laser ablation system (193 nm). Compared with the standard arrangement, the addition of nitrogen, in combination with the use of a newly designed X skimmer cone and Jet sample cone in the Neptune Plus, improved the signal intensities of Hf, Yb, and Lu by factors of 5.3, 4.0, and 2.4, respectively. All data were acquired on zircon in a single spot ablation mode with a spot size of 44 μm. For details on the operating conditions and analytical method, see Hu et al. (2008, 2012). The Hf isotope results are presented in Table S3 in supplementary material.

158 **4 Analytical results**

159 **4.1. Geochronology**

160 Zircon grains separated from 15 granitoid samples are euhedral-subhedral, with the
161 exception of sample 17JZ4-1 (monzonite), in which most zircon grains are xenomorphic granular.
162 All zircon grains display banded structures or oscillatory growth zoning, which is visible in
163 cathodoluminescence (CL) images. Th/U ratios are high (>0.2). All these observations are
164 indicative of a magmatic origin (Table S1; Belousova et al., 2002; Rubatto, 2002).
165 Representative zircon CL images are shown in Fig. 4.

166 The results show four groups of U–Pb zircon ages: ~261 Ma, 253–244 Ma, 183–175 Ma,
167 and 173–164 Ma. The oldest ages (~261 Ma) are found in a syenogranite pluton (sample 17JZ9-
168 1). This sample yielded zircon grains that are 100–180 μm long, with length/width ratios of 2:1–
169 3:1, and Th/U values of 0.61–1.60. A total of 24 analytical spots were conducted on 24 grains,
170 yielding 21 concordant ages. The weighted mean $^{206}Pb/^{238}U$ age is 261 ± 1 Ma (MSWD = 0.66, n
171 = 21). Three grains yielded slightly discordant ages due to the loss of radioactive Pb (Fig. 4a;
172 Table S1). The weighted mean age is interpreted as the age of crystallization.

173 Samples from a monzonite (sample 17JZ4-1) and quartz monzonite (sample 17JZ5-1)
174 pluton yielded zircon ages of 253–244 Ma. The zircon grains are 50–150 μm long, their
175 length/width ratios are 1:1–2:1, and their Th/U values are 0.46–1.06. All analytical spots for the
176 two samples yielded concordant ages (Fig. 4b, c; Table S1). The weighted mean $^{206}Pb/^{238}U$ ages
177 of 253 ± 2 Ma (MSWD = 0.49, n = 23) and 244 ± 2 Ma (MSWD = 0.94, n = 18) are interpreted
178 as the crystallization age of the monzonite and quartz monzonite, respectively.

179 Seven granitoid plutons and one diorite pluton yielded zircon ages of 183–175 Ma.
180 Granitoid samples included monzogranite (D1-7, 17JZ1-1 and 17JZ3-1), biotite monzogranite
181 (D5-1 and D15-1), two-mica monzogranite (17JZ2-1), and hornblende biotite-bearing

monzogranite (17JZ6-1). Zircon grains from these granitoids are 100 –230 μm long, their length/width ratios are 1.5:1–4:1, and their Th/U values are high (>0.22). Most of analytical spots yielded concordant ages, but a few slightly discordant ages were also obtained (possibly due to radioactive Pb loss) (Fig. 4). The minimum weighted mean $^{206}Pb/^{238}U$ ages of these granitoids, which range from 183 ± 1 Ma to 175 ± 2 Ma (Fig. 4d–j; Table S1), are interpreted as crystallization ages. Several zircon grains from samples D5-1 and D15-1 yielded older concordant ages (Fig. 4i and j), which are interpreted to represent the crystallization of inherited zircon entrained by these granitoids. Zircon grains from sample D6-1 (diorite) are 50–140 μm long, their length/width ratios are 1:1–3:1, and their Th/U values are 0.38–1.2. A total of 19 analytical spots were conducted on 19 grains, yielding 18 concordant $^{206}Pb/^{238}U$ ages of 175 ± 2 Ma (MSWD = 1.8, n = 13), 183 ± 2 Ma (MSWD = 0.21, n =2) and 203 ± 2 Ma (MSWD = 0.32, n = 3) (Fig. 4k; Table S1). One grain yielded concordant $^{206}Pb/^{238}U$ age of 233 ± 2 Ma. The weighted mean age of 175 ± 2 Ma is interpreted as the crystallization age of the diorite. The older ages are interpreted as crystallization ages of captured zircon grains entrained by the diorite.

Samples from five granitoid plutons yielded zircon ages of 173–164 Ma. The granitoids include biotite monzogranite (D1-1, 17JZ8-4, and D12-1), hornblende-bearing biotite monzogranite (D5-1 and D15-1) and syengranite (17JZ7-1). Zircon grains from these granitoids are 90–230 μm long, their length/width ratios are 2:1–4:1, and the Th/U values are 0.20–0.96 (Fig. 4l–p; Table S1). Most analytical spots yielded concordant ages, with minimum weighted mean $^{206}Pb/^{238}U$ ages that range from 173 ± 1 Ma to 164 ± 5 Ma (Fig. 4l–p; Table S1), which are interpreted as crystallization ages. Several zircon grains from samples D1-1 and D12-1 yielded older ages (Fig. 4l and p), which are interpreted to represent the crystallization of inherited zircon.

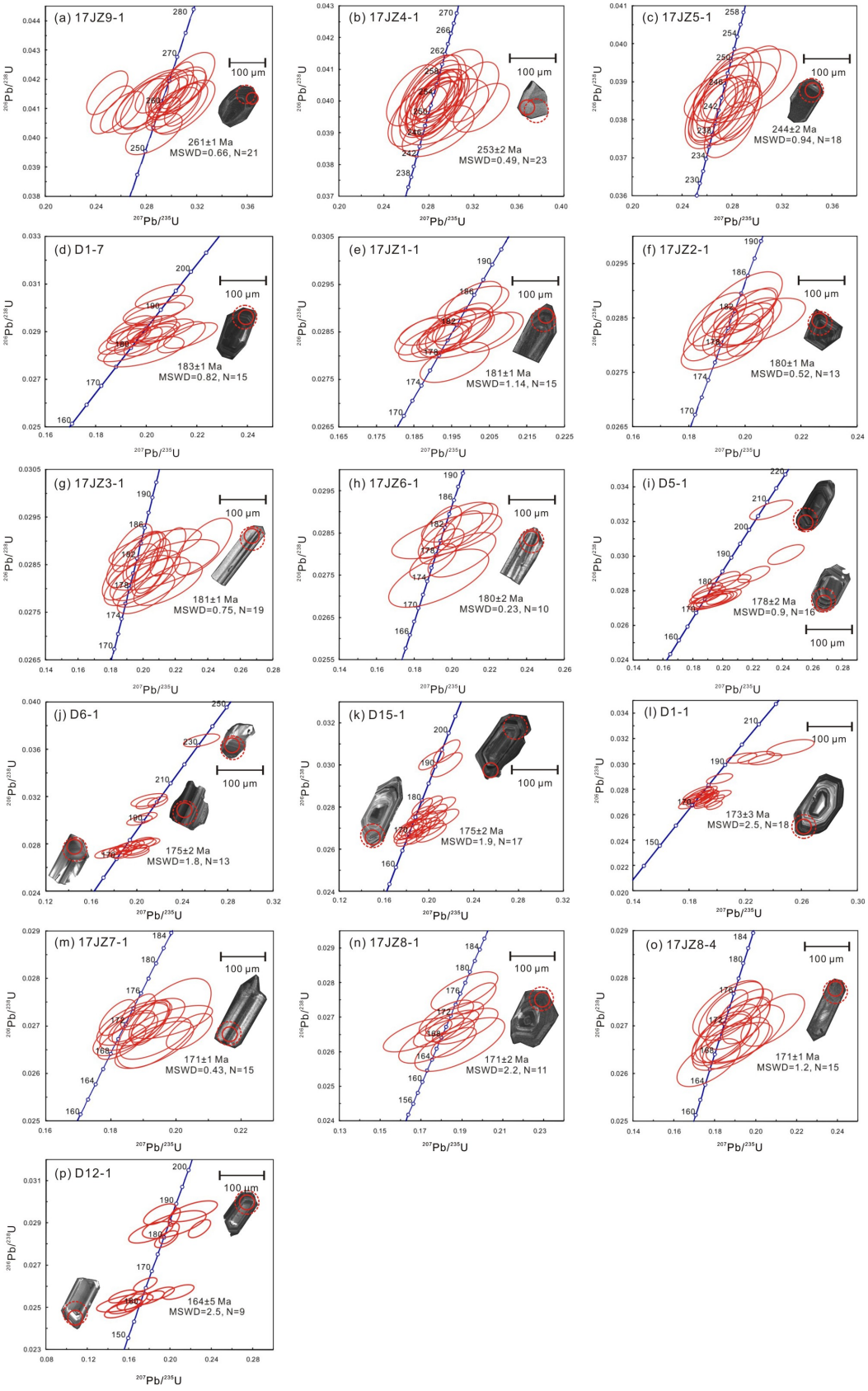
(a) 17JZ9-1
261±1 Ma
MSWD=0.66, N=21
(b) 17JZ4-1
253±2 Ma
MSWD=0.49, N=23
(c) 17JZ5-1
244±2 Ma
MSWD=0.94, N=18
(d) D1-7
183±1 Ma
MSWD=0.82, N=15
(e) 17JZ1-1
181±1 Ma
MSWD=1.14, N=15
(f) 17JZ2-1
180±1 Ma
MSWD=0.52, N=13
(g) 17JZ3-1
181±1 Ma
MSWD=0.75, N=19
(h) 17JZ6-1
180±2 Ma
MSWD=0.23, N=10
(i) D5-1
178±2 Ma
MSWD=0.9, N=16
(j) D6-1
175±2 Ma
MSWD=1.8, N=13
(k) D15-1
175±2 Ma
MSWD=1.9, N=17
(l) D1-1
173±3 Ma
MSWD=2.5, N=18
(m) 17JZ7-1
171±1 Ma
MSWD=0.43, N=15
(n) 17JZ8-1
171±2 Ma
MSWD=2.2, N=11
(o) 17JZ8-4
171±1 Ma
MSWD=1.2, N=15
(p) D12-1
164±5 Ma
MSWD=2.5, N=9
100 μm
$^{207}Pb/^{235}U$
$^{206}Pb/^{238}U$

206 **Figure 4.** Zircon U–Pb concordia diagrams and representative cathodoluminescence (CL)
207 images of selected zircons from the middle Permian to Middle Jurassic intrusive rocks.
208
209 **4.2. Major and trace element geochemistry**

210 Sample 17JZ9-1 (~261 Ma syenogranite) is characterized by high SiO_2 (73.83–74.53 wt.%),
211 low Al_2O_3 (13.76–13.94 wt.%), total Fe_2O_3 of 0.97–1.22 wt.%, MgO of 0.09–0.11 wt.%, and
212 CaO of 0.20–0.59 wt.%. Na_2O/K_2O ratios are 0.91–0.97 (Table S2). Plotted on total alkali *vs.*
213 SiO_2 (TAS) and K_2O *vs.* SiO_2 diagrams, the sample shows a subalkaline series and a high-K
214 calc-alkaline field, respectively (Fig. 5a, b). The values of A/CNK ($Al_2O_3/(CaO + K_2O + Na_2O)$)
215 are 1.02–1.08, indicating a weakly peraluminous composition (Fig. 5c). The sample shows
216 enrichment in light rare earth elements (LREE) and depletion in heavy rare earth elements
217 (HREE), with chondrite-normalized La/Yb (La/Yb_N) values of 13.10–14.67 (Table S2). In
218 addition, there is a negative Eu anomaly (δEu = 0.40–0.46), enrichment in large ion lithophile
219 elements (LILE; e.g., Rb and K), and depletion in Sr and high field strength elements (HFSE;
220 e.g., Nb, Ta, P and Ti) (Fig. 6a, b; Table S2).

221 Samples 17JZ4-1 (~253 Ma monzonite) and 17JZ5-1 (~244 Ma quartz monzonite) show
222 similar geochemical features, particularly for trace elements (Table S2; Figs. 5 and 6). They
223 contain low concentrations of SiO_2 (58.11–62.83 wt.%) and K_2O (1.44–2.53 wt.%), and
224 relatively high N_2O (4.00–5.03 wt.%). Plotted on the TAS diagram, they appear in the
225 subalkaline and calc-alkaline series (Fig. 5a, b). The values of Al_2O_3 (16.00–16.64 wt.%) and
226 CaO (4.41–6.43 wt.%) are relatively high, and the A/CNK values are 0.80–0.88, indicating a
227 metaluminous composition (Fig. 5c). The samples also show high contents of TiO_2 (0.67–0.88
228 wt.%), total Fe_2O_3 (4.51–6.39 wt.%), and MgO (3.01–4.59 wt.%). The samples are enriched in
229 LREEs and LILEs (e.g., Rb Ba and K), and depleted in HREEs and HFSEs (e.g., Nb, Ta, P and
230 Ti; Fig. 6b). They contain high concentrations of Sr (>632 ppm) and low concentrations of Y

(12.5 ppm). The values of Sr/Yb are relatively high (>54). The samples show negligibly negative to slightly positive Eu anomalies (δEu = 0.83–1.13) (Fig. 6a; Table S2).

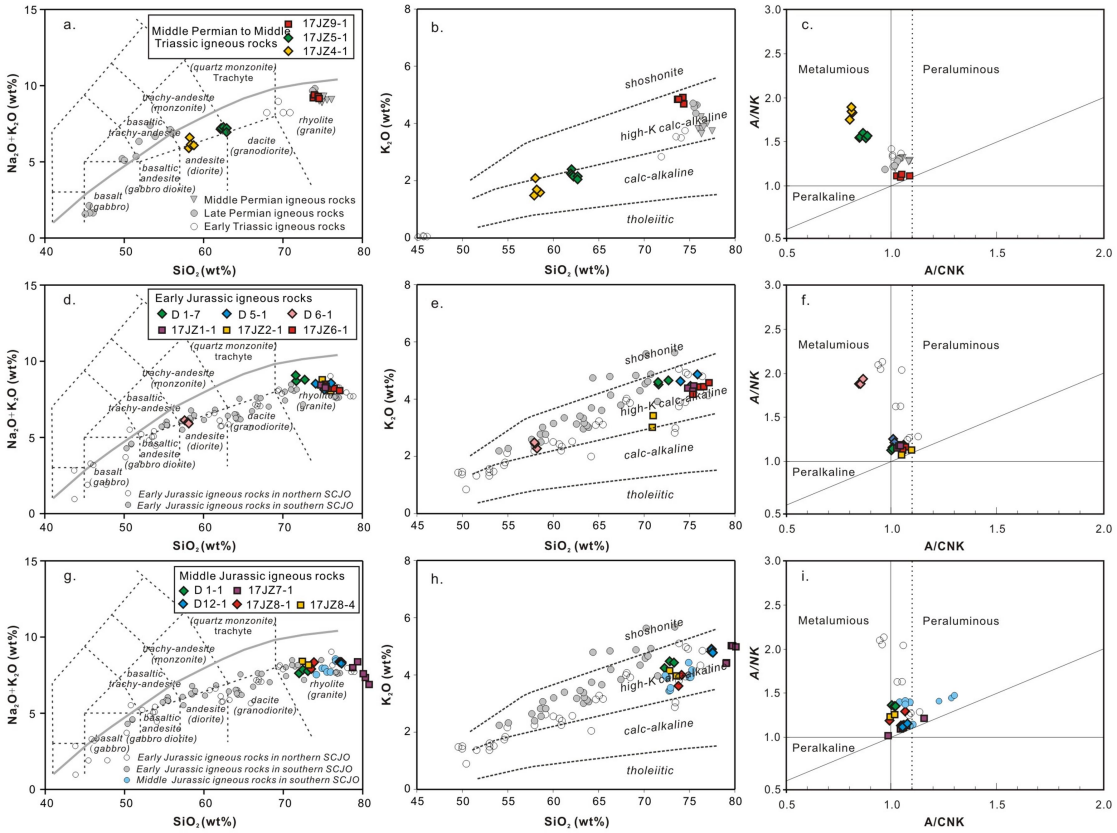

Figure 5. (a), (d), (g), and (j) Total alkali versus SiO_2 diagrams (TAS; after Irvine and Baragar, 1971); (b), (e), (h), and (k) K_2O versus SiO_2 diagrams (after Peccerillo and Taylor, 1976); (c), (f), and (i) A/NK ($Al_2O_3/(Na_2O + K_2O)$) versus A/CNK ($Al_2O_3/(CaO + K_2O + Na_2O)$) diagrams (after Maniar and Piccoli, 1989). The referenced samples for middle Permian to Middle Jurassic igneous rocks are from Cao et al., (2013), Pei et al., (2011), Wang et al., (2009, 2015, 2019) and Wu et al., (2002).

Granitoids samples dated 183–175 Ma (D1-7, 17JZ3-1, 17JZ1-1, D5-1, D15-1, 17JZ6-1, and 17JZ2-1) show similar major and trace element compositions (Table S2; Fig. 5 and 6). They have high concentrations of SiO_2 (70.74–77.14 wt.%) and low concentrations of Al_2O_3 (12.32–15.20 wt.%). Concentrations of other major elements are: total Fe_2O_3 (0.92–2.83 wt.%), MgO (0.10–0.77 wt.%), CaO (0.33–1.85 wt.%), Na_2O (3.52–4.46 wt.%), K_2O (2.97–4.93 wt.%), and

TiO_2 (0.07–1.31 wt.%) (Table S2). The compositions are associated with the subalkaline and high-K calc-alkaline series (Fig. 5d, e). Their low A/CNK values (1.00–1.09) are indicative of weakly peraluminous rocks (Fig. 5f). Trace element concentrations show enrichment in LREEs, depletion in HREEs ($(La/Yb)_N$=2.90–8.96), negative Eu anomalies (except of sample D5-1), enrichment in LILEs (e.g., Rb and K), and depletion in Ba, Sr and HFSEs (e.g., Nb, Ta, P and Ti) (Fig. 6c, d; Table S2).

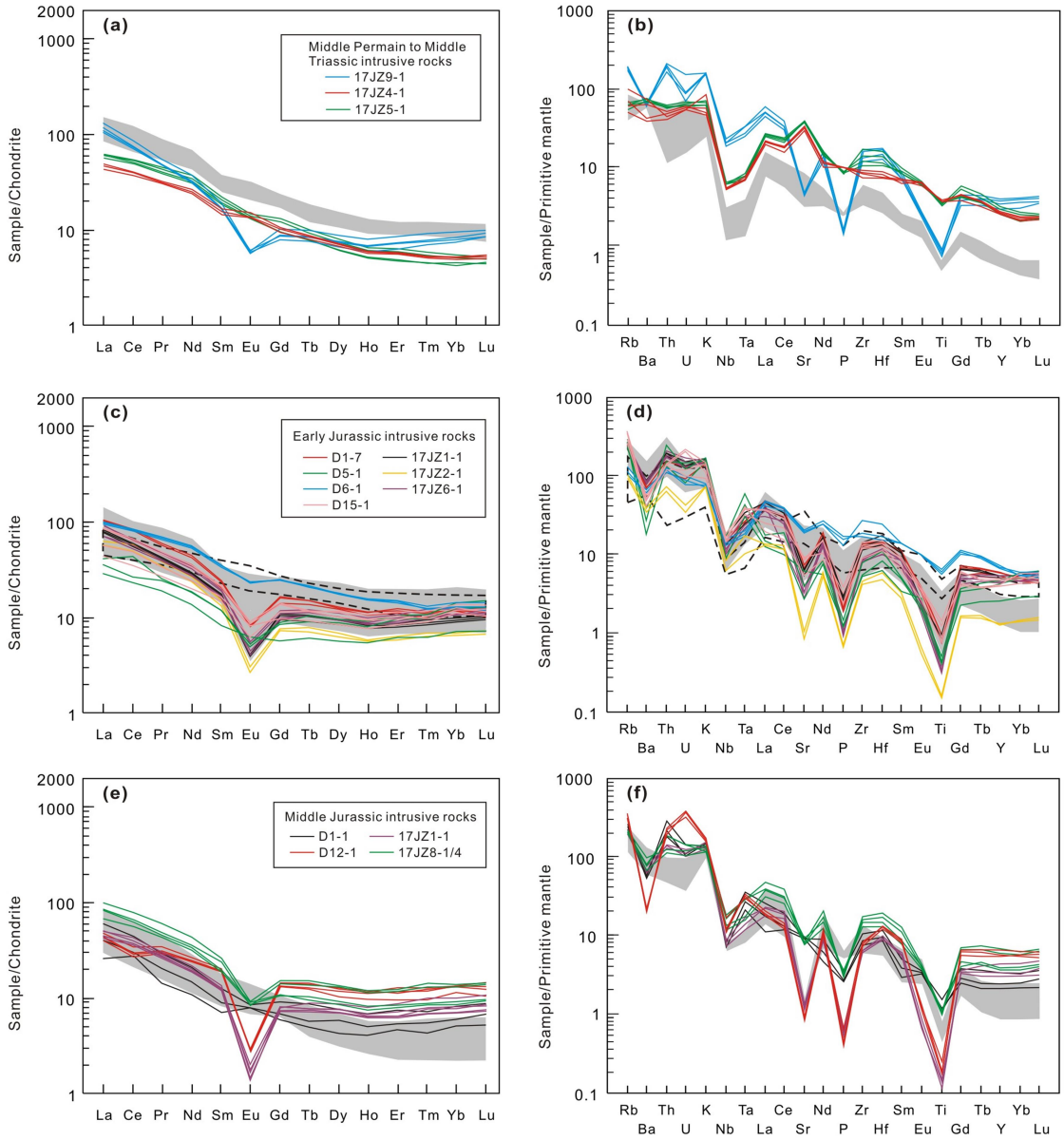

Figure 6. (a), (c), (e), and (g) Chondrite–normalized REE patterns diagrams; (b), (d), (f), and (h) Primitive mantle (PM) normalized trace element diagrams. The chondrite and PM values used for normalization are from Boynton (1984) and Sun and McDonough (1989), respectively. The shadow and dotted samples represent middle Permian to Middle Jurassic mafic and felsic rocks, respectively, which are from Cao et al., (2013), Pei et al., (2011), Wang et al., (2009, 2015, 2019) and Wu et al., (2002).

The ~175 Ma diorite sample (D6-1) is characterized by low concentrations of SiO_2 (57.68–58.10 wt.%), TiO_2 (1.18–1.31 wt.%), Na_2O (3.73–3.78 wt.%), and K_2O (2.22–2.41 wt.%), and high concentrations of Al_2O_3 (16.33–16.62 wt.%). The other major element concentrations are: total Fe_2O_3 (7.76–7.99 wt.%), MgO (2.91–3.04 wt.%), and CaO (5.68–5.74 wt.%) (Table S2). This rock belongs to the subalkaline and high-K calc-alkaline series (Fig. 5d, e). A/CNK values are low (0.85–0.87), indicating a metaluminous composition (Fig. 5f). The rock is enriched in LREEs and LILEs (e.g., Rb and K), and depleted in Ba, HREEs, and HFSEs (e.g., Nb, Ta, P and Ti) (Fig. 6d). It shows a negligible negative Eu anomaly (δEu = 0.74–0.81) (Fig. 6c; Table S2).

Granitoid samples dated 173–164 Ma (D1-1, 17JZ8-4, D12-1, 17JZ8-1, and 17JZ7-1) contain high concentrations of SiO_2 (72.20–81.09 wt.%) and low concentrations of TiO_2 (0.03–0.34 wt.%). Other major element concentrations are Al_2O_3 (10.78–14.14 wt.%), total Fe_2O_3 (0.13–2.56 wt.%), MgO (0.03–0.77 wt.%), CaO (0.20–1.99 wt.%), Na_2O (3.00–4.44 wt.%), and K_2O (3.49–4.89 wt.%) (Table S2). The rocks belong to the subalkaline series and high-K calc-alkaline field (Fig. 5g, h). A/CNK values are 0.97–1.15, indicative of metaluminous and weakly peraluminous rocks (Fig. 5i). Trace element concentrations show enrichment in LREEs and LILEs (e.g., Rb and K), and depletion in Ba, Sr, HREEs, and HFSEs (e.g., Nb, Ta, P and Ti). All samples, except of D1-1 and D1-2, show negative Eu anomalies (δEu = 0.14–0.58) (Fig. 6e; Table S2).

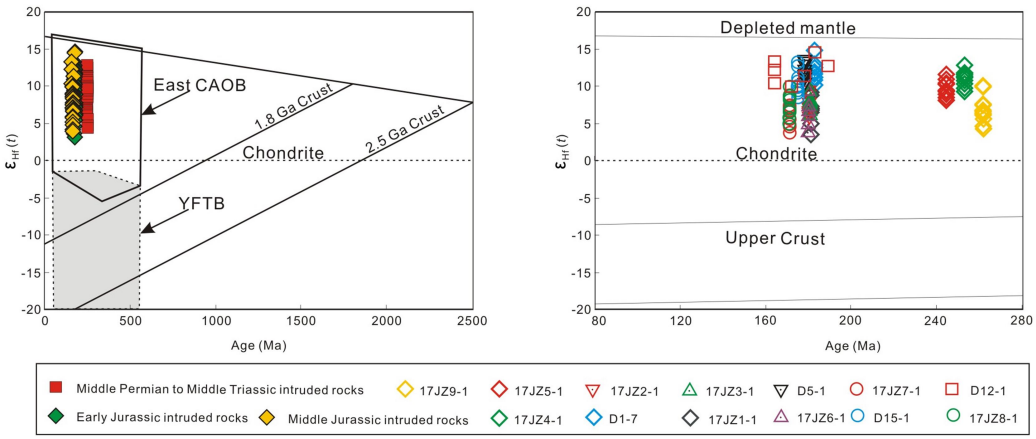

Figure 7. Correlations between Hf isotopic compositions and ages of zircons from the middle Permian to Middle Jurassic intrusive rocks. The Hf isotopic compositions of Eastern CAOB and Yanshan Fold and Thrust Belt (YFTB) are from Yang et al., (2006).

4.3. Zircon Hf isotopes

Results of *in situ* Hf isotope analyses are presented in Table S3 and Figure 7. Zircon grains dated ~261, ~253 and ~244 Ma yielded $^{176}Hf/^{177}Hf$ ratios of 0.282739–0.282972, and corresponding $\varepsilon_{Hf}(t)$ values of 4.2–8.9. The zircon grains from sample 17JZ9-1 (~261 Ma) yielded two-stage model ages (T_{DM2}) of 1016–645 Ma. Samples 17JZ4-1 (~253 Ma) and 17JZ5-1 (~244 Ma) yielded one-stage model ages (T_{DM1}) of 538–390 Ma and 563–418 Ma, respectively (Table S3; Fig. 7).

Primary zircon grains from granitoids dated 183–175 Ma yielded $^{176}Hf/^{177}Hf$ ratios of 0.282762–0.283082 and $\varepsilon_{Hf}(t)$ values of 3.3–14.7. T_{DM1} and T_{DM2} are 735–299 and 1014–343 Ma, respectively (Table S3; Fig. 7). Primary zircon grains from granitoids dated 171–164 Ma yielded $^{176}Hf/^{177}Hf$ ratios of 0.282785–0.283047 and $\varepsilon_{Hf}(t)$ values of 3.9–13.1. T_{DM1} and T_{DM2} are 701–296 and 970–345 Ma, respectively (Table S3; Fig. 7). Inherited zircon grains dated ~172, ~178, ~183 and ~189 Ma from sample D12-1 (~164 Ma monzogranite) yielded $^{176}Hf/^{177}Hf$ ratios of 0.282946 ($\varepsilon_{Hf}(t)$ = 9.8), 0.282984 ($\varepsilon_{Hf}(t)$ = 11.2), 0.283072 ($\varepsilon_{Hf}(t)$ = 14.4) and 0.283016 ($\varepsilon_{Hf}(t)$ = 12.6), respectively (Table S3; Fig. 7).

5. Discussion

5.1. Spatio-temporal distribution of the middle Permian to Middle Jurassic igneous rocks

Magmatism is a geological record of tectonic evolution, and their temporal switches often is response to convergent boundary process. Consequently, the spatio-temporal distribution of ignoues rocks can inform us on transitions in the tectonic regime. The development of the Suolunshan-Central Jilin Orogen was driven by subduction processes along the northern margin of the North China Craton (Li et al., 2006). The evolution of these subduction processes can be constrained by the spatio-temporal distribution of igneous rocks from this orogen.

Our geochronological results are generally consistent with results from previous studies in the Suolunshan-Central Jilin Orogen (Wu et al., 2011; Cao et al., 2013; Wang et al., 2015, 2019). Middle Permian to Middle Triassic igneous rocks have been reported from the eastern part of the Suolunshan-Central Jilin Orogen, represented by ca. 258 Ma olivine gabbro (Meihekou county), ca. 257 Ma monzogabbro (Gongzhuling city), ca. 259 Ma syenogranite (Liaoyuan county), ca. 255 Ma granodiorite, and ca. 249 Ma monzogranite (Siping city) (Fig. 2; Cao et al., 2013). Jurassic igneous rocks are widespread in the region and include mafic to felsic volcanic and intrusive rocks, particularly in the eastern part of the Suolunshan-Central Jinlin Orogen (Xu et al., 2009, 2013; Pei et al., 2011; Wu et al., 2011; Cao et al., 2013; Wang et al., 2015, 2017, 2019; Ma et al., 2017, 2018).

Based on the combination of new and published geochronological data (Table 1), we show that middle Permian to Middle Triassic magmatism in the area form an E-W trending belt along the northern margin of the North China Craton (Fig. 2; Wu et al., 2005). In contrast, the spatial distribution of Late Triassic and Jurassic igneous rocks generally follows a northeast–southwest trend (Fig. 2; Ma et al., 2017; Wang et al., 2019).

5.2. Petrogenesis and tectonic setting

The petrogenesis of igneous rocks can provide information on the tectonic setting during magmatism (Pearce et al., 1983; Maniar and Piccoli, 1989; Xu et al., 1999, 2013). Using our new petrographic and geochemical data, we discuss below the petrogenesis and inferred tectonic setting during each of the four phases of magmatism in the Suolunshan-Central Jilin Orogen.

5.2.1. Middle Permian (~261 Ma) magmatism

The earliest phase of magmatism is represented only by a single pluton of syenogranite dated ~261 Ma. Mechanisms that have been proposed to explain the origin of syenogranite include: (1) partial melting of crustal rocks (Whalen et al., 1987; Tchameni et al., 2001); (2) mixing of basaltic magma with crustal melt (Mingram et al., 2000; Vernikovsky et al., 2003; Macdonald et al., 2008); and (3) fractional crystallization of mantle-derived magmas (Litvinovsky et al., 2002; Wang et al., 2005; Nardi et al., 2008). In our study area, the syenogranite did not show evidence of mafic microgranular enclaves, acicular apatite, or plagioclase with reverse zoning, thus ruling out the possibility that it was derived from mixing of basaltic magma with crustal melt (Vernon, 1984; Mingram et al., 2000; Vernikovsky et al., 2003). In addition, the absence of coeval mafic magmatism in the study area indicates that it is unlikely that the syenogranite formed by fractional crystallization of mantle-derived magmas. It appears, therefore, that the intrusion was likely derived from a primary magma generated by partial melting of crustal material, thus explaining the high concentrations of SiO_2, Na_2O and K_2O, and the low concentrations of Fe_2O_3, MgO, and CaO.

The syenogranite yielded a high Th/La ratio of 0.44–0.50, which is consistent with lower continental crust material (Th/La >0.25; Plank, 2005). In addition, it contains relatively high concentrations of LREEs, and is relatively depleted in HREEs and in highly incompatible

341 elements (Ni, Ta, P, Ti, Ba and Sr) (Fig. 6). This depletion could either be attributed to the
342 source composition or to the presence of residual minerals in the source. The latter possibility is
343 more likely based on the evidence of the coupled variability of some associated elements (e.g.,
344 Eu and Sr) in the syenogranite and their inconsistency with the composition of the continental
345 crust (Rudnick and Gao, 2004). We therefore suggest that the presence of garnet and rutile as
346 residual phases was responsible for generating a primary magma that was depleted in HREEs
347 and HFSEs (Ni and Ta). Garnet and rutile control the partitioning of HREEs and HFSEs,
348 respectively. Furthermore, the presence of residual rutile also caused a strong negative Ti
349 anomaly. Other minerals that might have existed in residual phases are plagioclase and apatite.
350 Plagioclase can explain the depletion in Sr, the presence of a negative Eu anomaly, and the
351 relatively low CaO content (Tamura et al., 2011). The presence of apatite can account for the
352 depletion in P. Considering the ε_{Hf} (t) values (+4.2 to +10.0) and T_{DM2} ages (645 to 1016 Ma),
353 we suggest that the primary magma of the syenogranite was generated by partial melting of a
354 juvenile mafic lower crustal material, and the involvement of other crustal (e.g., Mesoproterozoic)
355 material in the source melts.

356 Coeval igneous rocks have not been found in study area, but syenogranite plutons dated
357 262–259 Ma are known from adjacent regions. These rocks belong to the high-K calc-alkaline
358 series and their geochemical features are akin to those described above (Cao et al., 2013). Based
359 on the petrogenesis and calc-alkaline affinity of these rocks, we suggest that this phase of
360 magmatism, at ca. 261 Ma, was developed in an active continental margin (Pitcher, 1993).

361 *5.2.2. Late Permian – Early Triassic (253–244 Ma) magmatism*

362 The monzonite (~253 Ma) and quartz monzonite (~244 Ma) plutons in the study area are
363 enriched in LREEs and depleted in HREEs. They are characterized by high concentrations of Sr,

364 low concentrations of Y and Yb, high Sr/Y ratios, and weakly positive Eu anomalies (Fig. 6;
365 Table S2). These characteristics are geochemically similar to adakite (Fig. 8a, b).

366 The following models have been suggested to explain the origin of adakitic magmas: (1)
367 partial melting of subducted oceanic crustal material (Defant and Drummond, 1990); (2) partial
368 melting of delaminated lower crust (Kay and Kay, 1993; Xu et al., 2002; Gao et al., 2004; Xu et
369 al., 2006); (3) partial melting of thickened mafic lower continental crust (Petford and Atherton,
370 1996; Chung et al., 2003; Wang et al., 2005); and (4) derivation by crustal assimilation and
371 fractional crystallization (AFC) processes from a basaltic parental magma (Castillo et al., 1999).

372 Adakite magmas generated by partial melting of thickened mafic lower continental crust
373 should have a high content of K_2O, a low Na_2O/K_2O ratio, low Mg#, and low concentrations of
374 MgO, Cr and Ni. Our samples have low concentrations of K_2O and high concentrations of MgO,
375 Cr and Ni, thus ruling out an origin via this mechanism. Likewise, it is unlikely that our samples
376 were derived from primary magmas generated lower-crustal delamination, because this process
377 is expected to produce high concentrations of Th (10–20 ppm) and high Th/La ratios (Plank,
378 2005). However, our samples contain relatively low Th concentrations (3.7 to 5.7 ppm). Melting
379 of thickened or delaminated lower crustal material is also unlikely in light of the absence of
380 inherited zircons in our samples (Fig. 4b, c). Geological and geochemical evidence also
381 precludes generation of adakite magmas by AFC, because these adakites does not exhibit linear
382 correlation of their composition, and no mafic pluton has been found in the study area.

383

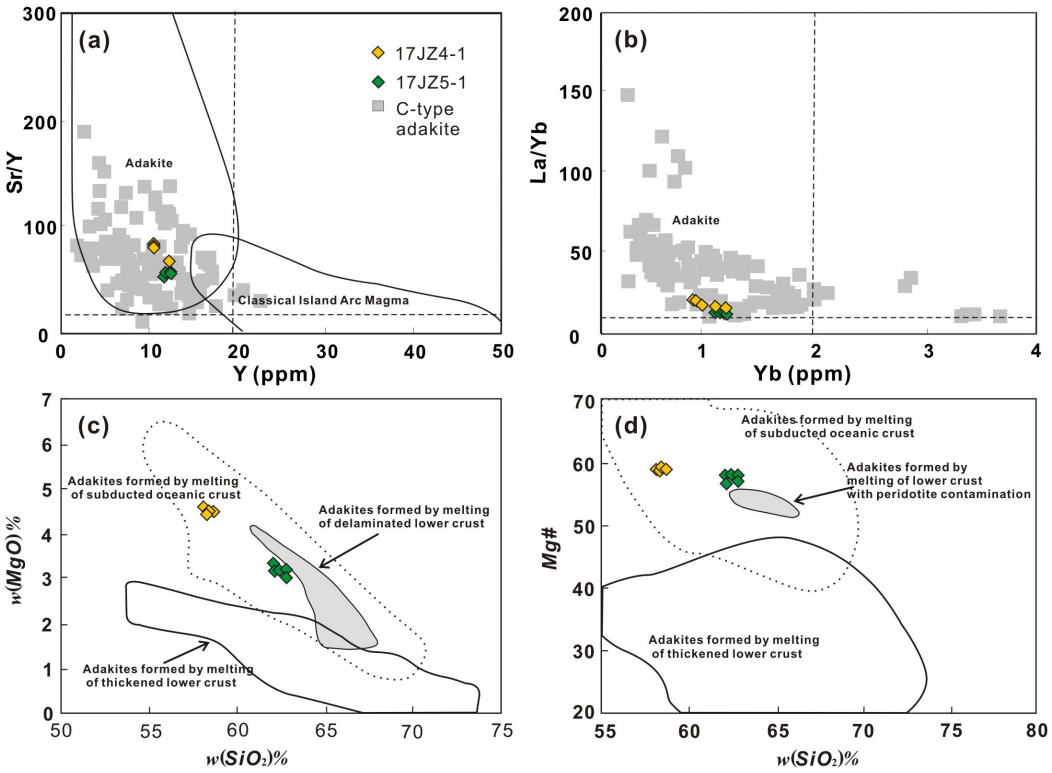

Figure 8. Discrimination diagrams of adakite. (a) Sr/Y versus Y diagram (after Martin, 2005); (b) La/Yb versus Yb diagram (after Moyen, 2009); (c) MgO versus SiO_2 diagram; (d) Mg# versus SiO_2 diagram. In Figs. 8a and b, the gray samples are C-type adakitic rocks within Eastern and Northern China from Moyen (2009) and references therein. In Fig. 8c, the adakites formed by melting of subducted oceanic crust are from Defant and Drummond (1990) and Martin (2005); the adakitic rocks formed by melting of thickened lower crust are from Atherton and Petford (1993) and Petford and Atherton (1996); and the adakitic rocks formed by melting of delaminated lower crust are from Xu et al. (2002). In Fig. 8d, the adakites formed by melting of subducted oceanic crust are from Defant and Drummond (1990) and Martin (2005); and the adakitic rocks formed by melting of lower crust with peridotite contamination and by melting of thickened lower crust are from Xiao et al. (2004).

The 253–244 Ma monzonite and quartz monzonite in the study area were likely formed by melting of subducted oceanic crustal material and the interaction of this melt with the overlying mantle wedge, which thus generated high concentrations of MgO, Cr and Ni (Defant and Drummond, 1990). This model is supported by discrimination diagrams for the genesis of

adakite (Fig. 8c, d). The zircon $\varepsilon_{Hf}(t)$ values of the adakites (8.2–12.6) suggest that they were generated by melting of a juvenile mafic material. Adakitic rocks occur in both island arcs and continental arcs, but magmas formed in continental arcs are commonly characterized by high Zr/Yb and Nb/Yb ratios (Miyashiro, 1974; Defant and Drummond, 1990; Pearce. 1996). Based on the geochemical data (Table S2), we suggest that the 253–244 Ma monzonite and quartz monzonite in the study area were associated with a continental magmatic arc.

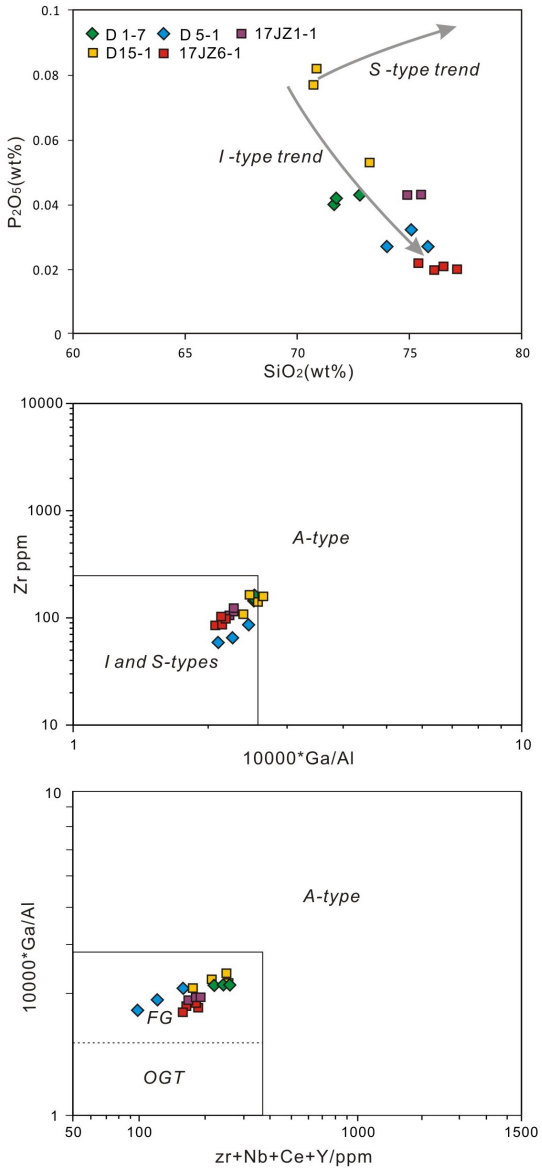

Fig. 9. Variations diagrams for Early Jurassic granitoids in study area. (a) the P_2O_5 versus SiO_2 diagram (after Whalen et al., 1987); (b) the Zr concentrations versus 10000*Ga/Al

discrimination diagram (after Chappell et al., 1999; Whalen et al., 1987); (c) the Zr + Nb + Ce + Y concentrations versus 10000*Ga/Al discrimination diagram (after Eby et al., 1990).

5.2.3. Early Jurassic (183–175 Ma) magmatism

Early Jurassic granitoids are mainly biotite monzogranites, characterized by high SiO_2, Na_2O and K_2O, low CaO, MgO and total Fe_2O_3, and variable Al_2O_3. Some of the plutons contain hornblende and secondary muscovite. The composition of the rocks corresponds to weakly peraluminous I-type granites, as indicate by the negative correlation between P_2O_5 and SiO_2 (Fig. 9a). A discrimination diagram based on Zr concentrations *vs* 10000*Ga/Al indicates that sample D15-1 might be an A-type granite. However, using the (Zr + Nb + Ce + Y) concentrations *vs* 10000*Ga/Al discrimination diagram, all samples are plotted in the I-type field, with sample 17JZ15-1 being highly fractionated I-type granite (Fig. 9b and c; Whalen et al., 1987; Chappell et al., 1999; Eby et al., 1990).

I-type granites are generally derived from igneous or meta-igneous sources (Whalen et al., 1987). The Early Jurassic granitoids in the study area are characterized by major element concentrations that are compatible with a process involving partial melting of crustal material, a conclusion that is also supported by the presence of inherited zircon grains and the wide range of zircon Hf isotopic composition (Figs 4 and 7; Table S3). The granitoids contains low concentrations of LREEs, and they are relatively depleted in HREEs and highly incompatible elements (Ni, Ta, P, Ti, Ba and Sr). Some samples are also depleted in La (Fig. 6). Melt generation was likely driven by subduction, and 'subduction components' (LREEs, Ba and Sr; Pearce et al., 2005) can provide information on the subduction processes. Generally, shallow subduction is characterized by enrichments in elements such as Ba, Rb and Sr, which are mobile in low-temperature aqueous fluids; in contrast, deep subduction is characterized by enrichments in the aforementioned elements and LREE as a result of sediment melting (Tamura et al., 2011).

The low concentrations of LREEs in the Early Jurassic granitoids indicate that that the primary magma did not experience metasomatism by sediment melting. The depleted concentrations of HREEs, Ni, P and Ti, suggest that garnet, rutile and apatite were present as residual phases (Tamura et al., 2011). In addition, based on the $\varepsilon_{Hf}(t)$ values (3.3–13.4), it is suggested that the magmas were generated by melting of juvenile lower continental crust. We therefore conclude that the origin of the Early Jurassic granitoids was associated with primary magmas that were generated by melting of juvenile lower continental crust.

In addition to the Early Jurassic granitoids, the study area also has a diorite body dated ~ 175 Ma. The following models have been suggested for the formation of dioritic magmas: (1) partial melting of mantle peridotite under water-saturated conditions (Hirose, 1997); (2) partial melting of subducting oceanic crust (Gerya and Yuen, 2003; Behn et al., 2011); (3) mixing of basaltic magma with crustal melt (Reubi and Blundy, 2009); and (4) fractional crystallization or AFC processes from a basaltic parental magma (Hildreth and Moorbath, 1988; Plank and Langmuir, 1988; Dai et al., 2016). The diorite in the study area is characterized by high contents of Al_2O_3, total Fe_2O_3, MgO and CaO, low contents of K_2O, and a low Na_2O/K_2O ratio. The diorite is enriched in LREEs but depleted in highly incompatible elements (Ni, Ta, P, Ti, Ba and Sr). Relative to mantle-derived magmas, the concentrations of MgO, Cr and Ni in the diorite are relatively low. Moreover, evidence that the diorite is enriched in LREEs indicates that it was unlikely derived from partial melting of mantle peridotite under water-saturated conditions, with refractory harzburgite as the residue (Grove et al., 2002). Intermediate magmas formed by melting of subducted oceanic crust are generally characterized by high Na_2O/K_2O ratios (averaging ~2.67), average Mg# values of 48, and Cr and Ni concentrations of 36 and 24 ppm, respectively (Defant and Drummond, 1990). Our data from the diorite sample (D6-1) are

457 inconsistent with these predictions (Table S3). Accordingly, the possibility that the diorite
458 formed by partial melting of mantle peridotite or by partial melting of subducting oceanic crust
459 can be ruled out.

460 Fractional crystallization and assimilation (AFC) commonly occur during magma ascent,
461 but crustal contamination in magma sources also plays an important role in the incorporation of
462 crustal components into mantle-derived magmas. Below, we first evaluate the roles of AFC
463 processes and then constrain the role of crustal contamination. Magma subjected to AFC
464 processes is expected to have enhanced concentrations of SiO_2 and melt-mobile incompatible
465 trace elements, such as Ba, Rb, Sr and Pb. In our data from sample D6-1, these elements show
466 irregular variations, thus indicating that the parental magma was unlikely subjected to AFC
467 processes (Table S2). Crustal contamination in the source is expected to enrich the parental
468 magma with LREEs and incompatible elements, but our data show that Ba and Sr are depleted in
469 the diorite sample (Fig. 6). It appears, therefore, that the ~175 Ma diorite in the study area was
470 unlikely derived from a basaltic parental magma that underwent fractional crystallization or AFC
471 processes. Considering the evidence of gabbroic fragments and amphibole-enriched haloes
472 surrounding the gabbroic fragments in the diorite, we suggest that the diorite most likely formed
473 from magma that was generated by mixing of basaltic magma with crustal melt.

474 In conclusion, Early Jurassic (183–175 Ma) igneous rocks in the study area belong to the
475 high-K calc-alkaline series and consist of andesite, rhyolite, syenogranite, monzogranite, and
476 diorite (Wang et al., 2019). The monzogranitic magmas were generated by melting of juvenile
477 lower continental crust, whereas diorite was most likely formed from magmas generated by
478 mixing of basaltic magma with crustal melt. The overall petrogenesis and high-K calc-alkaline

affinity of the igneous rocks are consistent with formation in a continental arc environment (Pitcher, 1997).

5.2.4. Middle Jurassic (173–164 Ma) magmatism

Middle Jurassic granitoids in the study area are characterized by high concentrations of SiO_2, Na_2O and K_2O, low concentrations of CaO, MgO and total Fe_2O_3, and variable concentrations of Al_2O_3. The A/CNK values and correlations between P_2O_5 and SiO_2 indicate that these granitoids are typically I-type. The major element signature and the presence of inherited zircon grains in these rocks indicate that they were generated by partial melting of crustal material. This conclusion is also supported by the wide range of zircon Hf compositions (Figs 4 and 7; Table S3).

Interestingly, the Middle Jurassic granitoids have variable concentrations of Eu, U, Sr, P, and Ti. Despite the different concentrations of Eu and Sr, the Eu–Sr coupling indicates a high oxygen fugacity of the parental magmas (Drake, 1975; Rowe et al., 2007; Wilke and Behrens, 1999). In addition, the presence of plagioclase as a residual mineral in the source played an important role during magma genesis under oxidizing conditions, thus resulting in variable concentrations of CaO. The variability in U contents and depletion in Ti and P might have resulted from the presence of apatite as a residual mineral. The $\varepsilon_{Hf}(t)$ values (3.9–13.1) suggest that these granitoids were generated by melting of juvenile lower continental crust. The collective petrographic and geochemical evidence, therefore, indicates that Middle Jurassic granitoids in the study area formed from primary magmas generated by melting of juvenile lower continental crust. These granitoids and coeval igneous rock assemblages, which belong to the high-K calc-alkaline series (Wang et al., 2019), were developed in an active continental margin.

5.3. Implication for a transition in the tectonic regime

The early history of the eastern part of the CAOB was influenced mainly by subduction of the Paleo-Asian Ocean. Following the consumption of this oceanic lithosphere and the establishment of new subduction systems at the Paleo-Pacific Ocean, a major transition in the tectonic regime affected the eastern CAOB. Scholars put forward different suggestions about the timing of tectonic overlying and transition. Our results provide new insights into the timing of this transition.

Late Permian to Middle Triassic intrusive rocks in our study area are characterized by positive zircon $\varepsilon_{Hf}(t)$ values. Such positive values are characteristic of the CAOB zircon grains, as opposed to zircons from the North China Craton, which typically have negative $\varepsilon_{Hf}(t)$ values (Yang et al., 2006; Fig. 7). We therefore suggest that the 261–244 Ma igneous rocks in our study area were intimately linked to orogenesis in the CAOB and hence to the subduction of the Paleo-Asian Ocean. In the area of Faku city, southwest of our study area, high-K adakite dated 227 ± 3 Ma has been found (Shi et al., 2019). Given that the generation of high-K adakite involves partial melting of thickened mafic lower continental crust, the evidence suggests that the Paleo-Asian Ocean was already consumed by ~227 Ma (Shi et al., 2019). Other Late Triassic (220–214 Ma) igneous rocks include a bimodal suite (hornblende gabbro, monzogranite, and granodiorite), associated with the high-K calc-alkaline series, which likely evolved during orogenic uplift and post-orogenic extension (Wu et al., 2011; Wang et al., 2019). This phase of magmatism, similar to the ~227 Ma adakite, postdated the termination of the Paleo-Asian Ocean subduction. Consequently, we conclude that the closure of the Paleo-Asian Ocean could occur between 244 Ma and 227 Ma.

523 Spatially, Late Triassic and Jurassic intrusive rocks are distributed from roughly northeast
524 to southwest (Fig. 2; Ma et al., 2017, 2019), which is a responding to tectonic regime transition
525 in the Late Triassic. There is an alkaline and ultrabasic complex belt extends east to west from
526 Liaoning province to inner Mongolia province along the northern margin of the North China
527 Craton, and with corresponding ages range from 250 to 219 Ma (Cao et al., 2013; Pei et al., 2008;
528 Peng et al., 2012; Wang et al., 2013, 2019; Wu et al., 2011). The eastern segment of the alkaline
529 and ultrabasic complex consist of ca. 222–219 Ma A-type granite and ultramafic rocks, which is
530 also a marker of tectonic transition from orogenic uplift to a post-orogenic extensional setting in
531 the Late Triassic (Cao et al., 2013; Wang et al., 2019).

532 The final closure of the Paleo-Asian Ocean is marked by the Solonker-Xar Moron-
533 Changchun-Yanji Suture. In segment of Changchun-Yanji, a belt of Carboniferous ophiolitic
534 mélange and deep-sea volcanic rocks in Yantongshan, Shuangyang and Toudaochuan area (Peng
535 et al., 1997), which likely represents relics of the Paleo-Asian Ocean (Xiao et al., 2003; Li, 2006).
536 Cao et al. (2019) have recently suggested that high-pressure metamorphism in the Yantongshan
537 ophiolitic mélange occurred after 237 Ma. Furthermore, mylonites from a ductile shear zone near
538 Yanji city yielded ^{40}Ar-^{39}Ar ages of 230–227 Ma (Peng et al., 2012 and references therein).
539 These metamorphic ages might represent a phase of deformation and metamorphism following
540 the final closure of the Paleo-Asian Ocean, further supporting our suggestion that a change in the
541 tectonic regime could occur at ca. 237–227 Ma.

542 Paleontological and stratigraphic studies support the idea that a change in the tectonic
543 regime occurred during the Late Triassic. Some authors have suggested that the final closure of
544 the Paleo-Asian Ocean occurred already in the late Permian, based on the recognition that marine
545 volcano-sedimentary Permian strata gradually change into supposedly late Permian continental

facies (Li et al., 2006, Zhou et al., 2017a). However, this interpretation seems incorrect, as indicated by the occurrence of marine fossil communities and marine interlayers in the late Permian strata (Peng et al., 2012 and references therein). Marine fossils were also found in black shale from the Early Triassic Lujiatun Formation, which is unconformably overlain by Late Triassic strata (Peng et al., 2012 and references therein). This unconformity between Early and Late Triassic strata might be associated with the final closure of the Paleo-Asian Ocean. Elsewhere, the Early Triassic strata are overlain by Middle Triassic marine volcano-sedimentary rocks with carbonate interlayers (e.g., Kedao Formation deposited in 241–233 Ma; JBGMB, 1988; Zhou et al., 2017b). Late Triassic strata are associated with volcano-sedimentary rocks and coal seams (e.g., Dajianggang Fm with maximum depositional age of ~217 Ma; Zhou et al., 2017b). It appears, therefore, that the sedimentary environment gradually changed from marine to continental facies during the Triassic, supporting our conclusion that the final closure of the Paleo-Asian Ocean occurred during late stage of Middle Triassic or early stage of Late Triassic.

In conclusion, the integrated evidence from igneous petrology, metamorphic petrology, structural geology, paleontology and stratigraphy suggests that the timing of tectonic regime transition occurred in late stage of Middle Triassic or early stage of the Late Triassic (244–227 Ma).

5.4. Tectonic evolution of the Changchun-Yanji Suture

The Changchun-Yanji Suture marks the easternmost location of the Paleo-Asian Ocean closure and provides information on the tectonic evolution of the Suolunshan-Central Jilin Orogen. Following the final closure of the Paleo-Asian Ocean at 244–227 Ma, the area was affected by Late Triassic (223–214 Ma) bimodal igneous rocks, which were possibly linked to long episodes of contraction intermitted by a shorter period of crustal extension. As recorded by

569 Jurassic igneous rocks, 190–185 Ma alkaline and bimodal igneous rocks indicate study area
570 remained an extensional environment. In contrast, 185–175 Ma granitoids, diorites, andesites and
571 rhyolites are middle- to high-K calc-alkaline rocks and formed in a continental arc environment
572 (Fig. 5a, b), which were likely developed during the early stages of subduction (Pitcher, 1997;
573 Wu et al., 2002, 2011). In addition, a N–S trending Heilongjiang accretionary complex formed in
574 188–177 Ma along the Jiayin-Mudanjiang Fault, and it was considered as produce of subduction
575 of the Paleo-Pacific Ocean (Sun et al., 2018). Therefore, the spatio-temporal coupling between
576 Early Jurassic magmatism and Heilongjiang accretionary complex lend support to our hypothesis
577 that tectonic regime transition from the influence of Paleo-Asian Ocean convergence to the
578 subduction of the Paleo-Pacific Ocean occurred between Late Triassic and Early Jurassic (223–
579 185 Ma).

580 Subsequently, the tectonic evolution of the easternmost part of the Suolunshan-Central Jilin
581 Orogen was controlled mainly by subduction of the Paleo-Pacific Ocean. The widespread Middle
582 Jurassic (173–164 Ma) and dotted Late Jurassic (163–158 Ma) igneous rocks were possibly part
583 of a magmatic arc along the active continental margin. Their distribution range suggests that the
584 speed was decreasing gradually as the subduction evolved. The lack of 157–140 Ma magmatism
585 in the easternmost part of the CAOB further is indicative of a probable intermission of
586 subduction. The tectonic evolution history during Middle and Late Jurassic was also recorded by
587 Raohe complex, which consists of 216–166 Ma intraoceanic igneous rocks in an accretionary
588 prism overlain by terrestrial clastic sediments (Sun et al., 2015). These intraoceanic igneous
589 rocks derived from oceanic slab can be interpreted as subduction of the Paleo-Pacific Ocean,
590 whereas the provenance of overlying terrestrial clastic deposits can provide effectively constraint
591 for tectonic evolution of study area. The detrital zircons U-Pb dating and Hf isotopic analysis

indicate that all 155–140 Ma zircon grains derived from the North China Craton, and further proves the existent of the intermission during late stage of Late Jurassic. Therefore, the Changchun-Yanji Suture experienced multiple tectonic mode switches from Late Paleozoic to Mesozoic, and was controlled by westward (present-day coordinates) subduction of the Paleo-Pacific Ocean since Early Jurassic.

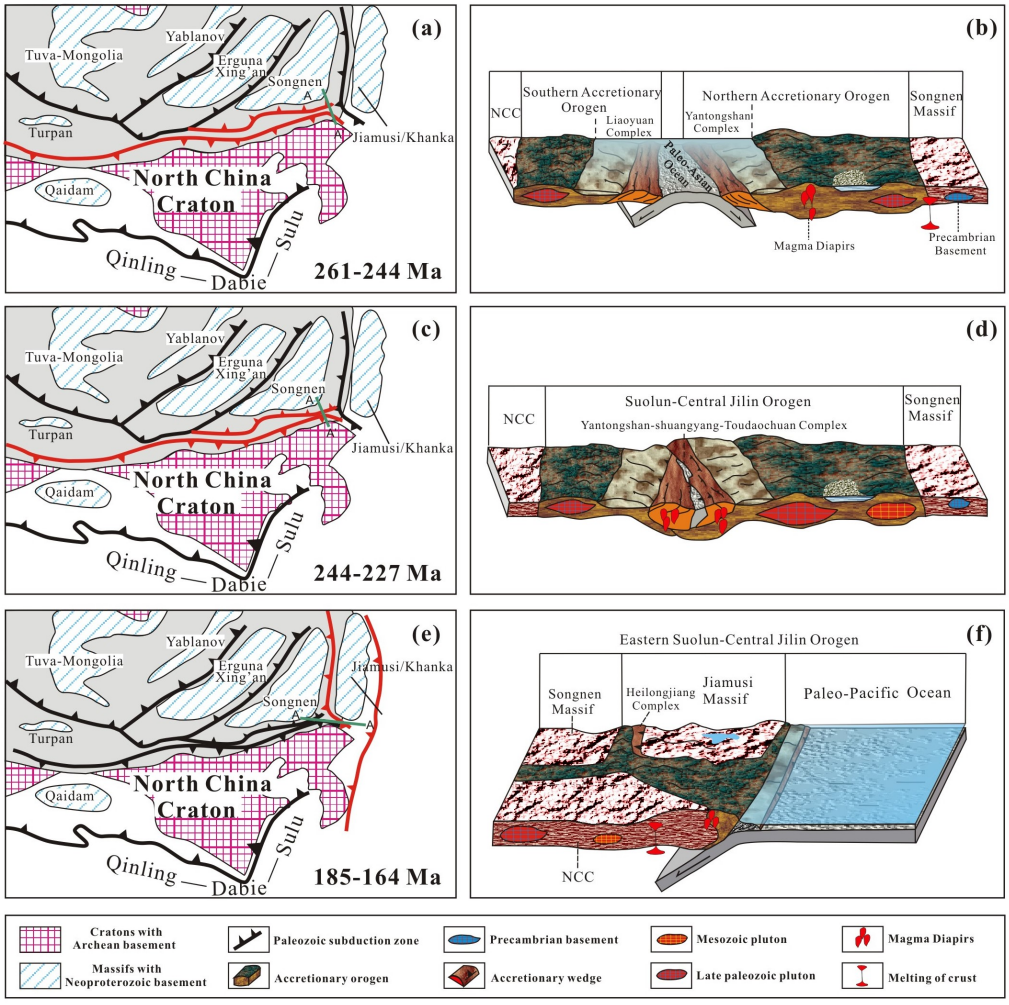

Fig. 10. Scenario for the middle Permian to Middle Jurassic tectonic evolution of the Changchun-Yanji Suture.

Our schematic tectonic reconstruction (Fig. 10) assumes that middle Permian to Middle Triassic contraction was ultimately controlled by double-sided subduction of the Paleo-Asian Ocean (Fig. 10a, b). Following the final closure of the Paleo-Asian Ocean, at late stage of Middle

603 Triassic or early stage of Late Triassic, Carboniferous ophiolitic mélange and deep-sea volcanic
604 rocks were emplaced at the suture zone (Fig. 10c, d). At 223–185 Ma, contraction was disrupted
605 by a shorter period of crustal extension. Subsequently, subduction of the Paleo-Pacific Ocean
606 resulted in widespread 185–164 Ma magmatism and the development of Heilongjiang
607 accretionary complex (Fig. 10e, f).

608 **6 Conclusions**

609 Based on zircon U–Pb ages and geochemical data, the following conclusions are drawn.

610 1. Middle Permian to Middle Jurassic igneous rocks in the area of Jilin were emplaced
611 during four major phases, at ca. 261 Ma, 253–244 Ma, 183–175 Ma, and 173–164 Ma.

612 2. The earliest phase of magmatism, at ca. 261 Ma, was generated in an active continental
613 margin by partial melting of juvenile mafic lower crustal material. Magmatism at 253–244 Ma
614 was generated in a continental arc environment by partial melting of juvenile mafic subducted
615 oceanic crust. At 183–175 Ma, monzogranitic and dioritic magmas were generated in a
616 continental arc environment via melting of juvenile lower continental crust and mixing of
617 basaltic magma with crustal melt, respectively. The final stage of magmatism, at 173–164 Ma,
618 formed in an active continental margin, generated by melting of juvenile lower continental crust.

619 3. Integrated evidence suggests that the closure of the Paleo-Asian Ocean could occur at
620 244–227 Ma, whereas the timing of tectonic regime transition from the influence of Paleo-Asian
621 Ocean subduction to the subduction of the Paleo-Pacific Ocean occurred between Late Triassic
622 and Early Jurassic (223–185 Ma).

623 4. The Changchun-Yanji Suture experienced multiple tectonic mode switches from Late
624 Paleozoic to Mesozoic, and was controlled by subduction of the Paleo-Pacific Ocean since Early
625 Jurassic.

Acknowledgments

We thank the staff of the State Key Laboratory of Geological Processes and Mineral Resources, China University of Geosciences, for their advice and assistance during zircon LA–ICP–MS U–Pb dating, major and trace element analyses, and Hf isotope analyses. This work was financially supported by the National Key Basic Research Program of China (2017YFC0601304) and the National Natural Science Foundation of China (Grants 91858211, 41972053). All data are archived at Mendeley Date (http://dx.doi.org/10.17632/383sjsrmtf.1).

References

Anderson, T. (2002). Correction of common Lead in U–Pb analyses that do not report ^{204}Pb. *Chemical Geology,* 192, 59 – 79.

Atherton, M.P. & Petford, N. (1993). Generation of sodium-rich magmas from newly underplated basaltic crust. *Nature*, 362, 144–146.

Behn, M. D., Kelemen, P. B., Hirth, G., Hacker, B. R. & Massonne, H. J. (2011). Diapirs as the source of the sediment signature in arc lavas. *Nature Geoscience*, 4, 641–646.

Belousova, E.A., Griffin,W.L., O'Reilly, S.Y. & Fisher, N.I. (2002). Igneous zircon: trace element composition as an indicator of source rock type. *Contributions to Mineralogy and Petrology*, 143, 602 – 622.

Boynton, W.V. (1984). Geochemistry of the rare earth elements: meteorite studies. In: Henderson, P. (Ed.), *Rare Earth Element Geochemistry*. Elsevier, Amsterdam, pp. 63–114.

Cao, J.L., Zhou, J.B. & Li, L. (2019). The tectonic evolution of the Changchun-Yanji suture zone: Constraints of zircon U-Pb ages of the Yantongshan accretionary complex (NE China). *Journal of Asian Earth Science*, Doi.org/10.1016/j.jseaes.2019.104110.

Cao, H.H., Xu, W.L., Pei, F.P., Wang, Z.W., Wang, F. & Wang, Z.J. (2013). Zircon U-Pb geochronology and petrogenesis of late Paleozoic-Early Mesozoic intrusive rocks in the eastern segment of the northern margin of the North China Block. *Lithos*, 170-171, 191-207.

Castillo, P.R., Janney, P.E. & Solidum, R.U. (1999). Petrology and geochemistry of Camiguin island, southern Philippines: insights to the source of adakites and other lavas in a complex arc setting. *Contributions of Mineralogy and Petrology*, 134, 33–51.

Chappell, B.W. (1999). Aluminium saturation in I and S-type granites and the characterization of fractionated haplogranites. *Lithos*, 46, 535–551.

Chung, S.L., Liu, D.Y., Ji, J.Q., Chu, M.F., Lee, H.Y., Wen, D.J., Lo, C.H., Lee, T.Y., Qian, Q. & Zhang, Q. (2003). Adakites from continental collision zones: melting of thickened lower crust beneath southern Tibet. *Geology*, 31, 1021–1024.

Dai, F.Q., Zhao, Z.F., Dai, L.Q. & Zheng, Y.F. (2016). Slab-mantle interaction in the petrogenesis of Andesitic magmas: Geochemical evidence from postcollisional intermediate volcanic rocks in the Dabie Orogen, China. *Journal of Petrology*, 06, 1–26.

Defant, M.J. & Drummond, M.S. (1990). Derivation of some modern arc magmas by melting of young subducted lithosphere. *Nature*, 34, 662–665.

Drake, M. J. (1975). The oxidation state of europium as an indicator of oxygen fugacity. *Geochimica et Cosmochmica Acta*, 39, 55–64.

Eby, G.N. (1990). The A-type granitoids: A review of their occurrence and chemical characteristics and speculations on their petrogenesis. *Lithos*, 26, 115–134.

Eizenhöfer, P.R., Zhao, G.C., Zhang, J. & Sun, M. (2014). Final closure of the Paleo-Asian Ocean along the Solonker Suture Zone: Constraints from geochronological and geochemical data of Permian volcanic and sedimentary rocks. *Tectonics*, 33, 441 – 463.

671 Gao, S., Rudnick, R.L., Yuan, H.L., Liu, X.M., Liu, Y.S., Xu, W.L., Lin, W.L., Ayers, J., Wang,
672 X.C. & Wang, Q.H. (2004). Recycling lower continental crust in the North China craton.
673 *Nature*, 432, 892–897.
674 Gerya, T. V. & Yuen, D. A. (2003). Rayleigh–Taylor instabilities from hydration and melting
675 propel 'cold plumes' at subduction zones. Earth and Planetary Science Letters 212, 47–62.
676 Grove, T., Parman, S., Bowring, S., Price, R. & Baker, M. (2002). The role of an H_2O-rich fluid
677 component in the generation of primitive basaltic andesites and andesites from the Mt.
678 Shasta region, N California. *Contributions to Mineralogy and Petrology*, 142, 375–396.
679 Han, J., Zhou, J.B., Li, L. & Song, M.C. (2017). Mesoproterozoic (~1.4 Ga) A-type Gneisseic
680 Granites in the Break-up of Columbia in the Eastern CAOB. *Precambrian Research*, 296,
681 20 – 38.
682 Hildreth, W. & Moorbath, S. (1988). Crustal contributions to arc magmatism in the Andes of
683 central Chile. *Contributions to Mineralogy and Petrology*, 98, 455–489.
684 Hirose, K. (1997). Melting experiments on lherzolite KLB-1 under hydrous conditions and
685 generation of high-magnesian andesites. *Geology*, 25, 42–44.
686 Hu, Z.C., Liu, Y.S., Gao, S., Hu, S.H., Dietiker, R. & Günther, D. (2008). A local aerosol
687 extraction strategy for the determination of the aerosol composition in laser ablation
688 inductively coupled plasma mass spectrometry. *Journal of Analytical Atomic Spectrometry*,
689 23, 1192 – 1203.
690 Hu, Z.C., Liu, Y.S., Gao, S., Liu, W.G., Yang, L., Zhang, W., Tong, X.R., Lin, L., Zong, K.Q.,
691 Li, M., Chen, H.H. & Zhou, L. (2012). Improved in situ Hf isotope ratio analysis of zircon
692 using newly designed X skimmer cone and Jet sample cone in combination with the

addition of nitrogen by laser ablation multiple collector ICP-MS. *Journal of Analytical Atomic Spectrometry*, 27, 1391 – 1399.

Irvine, T.H. & Baragar, W.R.A. (1971). A guide to the chemical classification of the common volcanic rocks. *Canadian Journal of Earth Sciences*, 8, 523–548.

Jahn, B.M., Wu, F.Y. & Chen, B. (2000). Massive granitoid generation in central Asia: Nd isotopic evidence and implication for continental growth in the Phanerozoic. *Episodes*, 23, 82 –92.

JBGMR (Jilin Bureau of Geology and Mineral Resources), (1997). *Stratigraphy (Lithostatic) of Jilin Province (in Chinese)*. China University of Geosciences Press, Wuhan, pp. 10–13.

Kay, R.W. & Kay, S.M. (1993). Delamination and delamination magmatism. *Tectonophysics*, 219, 177–189.

Khanchuk, A.I., Vovna, G.M., Kiselev, V.I., Mishkin, M.A. & Lavrik, S.N. (2010). First results of zircon LA-ICP-MS U-Pb dating of the rocks from the Granulite Complex of Khanka Massif in the Primorye region. *Doklady Earth Sciences*, 434 (1), 1164–1167.

Li, J.Y. (2006). Permian geodynamic setting of Northeast China and adjacent regions: Closure of the Paleo-Asian Ocean and subduction of the Paleo-Pacific Plate. *Journal of Asian Earth Sciences*, 26, 207–224.

Li, Y., Ding, L.L., Xu, W.L., Wang, F., Tang, J., Zhao, S. & Wang, Z.J. (2015). Geochronology and geochemistry of muscovite granite in Sunwu area, NE China: Implications for the timing of closure of the Mongol-Okhosk Ocean. *Acta Petrologica Sinica*, 31, 56–66 (in Chinese with English abstract).

714 Li, Y., Xu, W.L., Zhu, R.X., Wang, F., Ge, W.C. & Sorokin, A.A. (2020). Late Jurassic to Early
715 Cretaceous tectonic nature on NE Asia continental margin: Constraints from Mesozoic
716 accretionary complexes. *Earth-Science Reviews*, 200, 103042.
717 Litvinovsky, A.A., Jahn, B.M., Zanvilevich, A.N., Saunders, S., Poulain, S., Kuzmin, D.V.,
718 Reichow, M.K. & Titov, A.V. (2002). Petrogenesis of syenite-granite suites from the
719 Bryansky Complex (Transbaikalia, Russia): implications for the origin of A-type granitoids
720 magmas. *Chemical Geology*, 189, 105 – 133.
721 Liu, Y.S., Gao, S., Hu, Z.C., Gao, C.G., Zong, K.Q. & Wang, D.B. (2010). Continental and
722 oceanic crust recycling-induced melt-peridotite interactions in the Trans-North China
723 Orogen: U–Pb dating, Hf isotopes and trace elements in zircons of mantle xenoliths.
724 *Journal of Petrology*, 51, 537–571.
725 Luan, J.P., Wang, F., Xu, W.L., Ge, W.C., Sorokin, A.A., Wang, Z.W. & Guo, P. (2017a).
726 Provenance, age, and tectonic implications of Neoproterozoic strata in the Jiamusi Massif:
727 evidence from U–Pb ages and Hf isotope compositions of detrital and magmatic zircons.
728 *Precambrian Research*, 297, 17–32.
729 Luan, J.P., Xu, W.L., Wang, F., Wang, Z.W. & Guo, P. (2017b). Age and geochemistry of
730 Neoproterozoic granitoids in the Songnen–Zhangguangcai Range Massif, NE China:
731 Petrogenesis and tectonic implications. *Journal of Asian Earth Sciences*, 148, 265–276.
732 Luan, J.P., Yu, J.J., Yu, J.L., Cui, Y.C. & Xu, W.L. (2019). Early Neoproterozoic magmatism
733 and associated metamorphism in the Songnen Massif, NE China: Petrogenesis and tectonic
734 implications. *Precambrian Research*, 328, 250–268.
735 Ludwig, K.R. (2003). ISOPLOT 3: a geochronological toolkit for microsoft excel. *Berkeley*
736 *Geochronology Centre Special Publication*, 4, 74.

737 Ma, X.H., Zhu, W.P., Zhou, Z.H. & Qiao, S.L. (2017). Transformation from Paleo-Asian Ocean
738 clousure to Paleo-Pacific subduction: New constraints from granitoids in the eastern Jilin-
739 Heilongjiang Belt, NE China. *Journal of Asian Earth Sciences*, 144, 261–286.
740 Ma, X.H., Chen, C.J., Zhao, J.X., Qiao, S.L. & Zhou, Z.H. (2019). Late Permian intermediate
741 and felsic intrusions in the eastern Central Asian Orogenic Belt: Final-stage magmatic
742 record of Paleo-Asian Ocean subduction? *Lithos*, 326-327, 265–278.
743 Macdonald, R., Belkin, H.E., Fitton, J.G., Rogers, N.W., Nejbert, K., Tindle, A.G. & Marshall,
744 A.S. (2008). The roles of fractional crystallization, magma mixing, crystal mush
745 remobilization and Volatile- melt interactions in the genesis of a young basalt-peralkaline
746 rhyolith suite, the Great Olkaria Volcanic Complex, Kenya Rift Valley. *Journal of*
747 *Petrology*, 49 (8), 1515 – 1547.
748 Maniar, P.D. & Piccoli, P.M. (1989). Tectonic discrimination of granitoids. *Geological Society*
749 *of American Bulletin*, 101, 635–643.
750 Martin, H., Smithies, R.H., Rapp, R., Moyen, J.F. & Champion, D. (2005). An overview of
751 adakite, tonalite-tondhjemite-granodiorite (TTG), and sanukitoid: relationships and some
752 implications for crustal evolution. *Lithos*, 79, 1–24.
753 Mayshiro, A. (1974). Volcanic rock series in island arcs and active continental margins.
754 *American Journal of Science*, 274, 321–355.
755 Mingram, B., Trumbull, R.B., Littman, S. & Gerstenberger, H. (2000). A petrogenetic study of
756 androgenic felsic magmatism in the Cretaceous Paresis ring complex, Namibia: evidence
757 for mixing of crust and mantle-derived components, *Lithos*, 54, 1 – 22.
758 Moyen, J.F. (2009). High Sr/Y and La/Yb ratios: A meaning of the “adakitic signature”. *Lithos*,
759 112, 556–574.

760 Nardi, L.V.S., Placid, J., Bitencourt, M.D.F. & Stabel, L.Z. (2008). Geochemistry and
761 petrigenesis of post-collisional ultrapotassic syenites and granites from southernmost Brazil:
762 the Piquiri Syenite Massif. *Annals of the Brazilian Academy of Sciences*, 80 (2), 353 – 371.
763 Peccerillo, A. & Taylor, A.R. (1976). Geochemistry of Eocene calc-alkaline volcanic rocks from
764 the Kastamonu area, Northern Turkey. *Contributions to Mineralogy and Petrology*, 58 (1),
765 63 –81.
766 Pearce, J.A. (1983). The role of sub-continental lithosphere in magma genesis at destructive plate
767 margins. In: Hawkesworth, C.J., Norry, M.J., (Eds.), *Continental Basalts and Mantle*
768 *Xenoliths, Nantwich, Shiva*, pp. 230–249.
769 Pearce, J.A. (1996). Source and settings of granitic rocks. *Episodes*, 19, 120–125.
770 Pearce, J. A., Stern, R. J., Bloomer, S. H. & Fryer, P. (2005). Geochemical mapping of the
771 Mariana arc^basin system: implications for the nature and distribution of subduction
772 components. *Geochemistry, Geophysics, Geosystems*, 6 (7), 1–27.
773 Pei, F.P., Xu, W.L., Yu, Y., Zhao, Q.G. & Yang, D.B. (2008). Petrogenesis of the Late Triassic
774 Mayihe Pluton in Southern Jilin province: evidence from zircon U-Pb Geochronology and
775 Geochemistry. *Journal of Jilin University (English Science Edition)*, 38 (3), 351–362.
776 Pei, F.P., Xu, W.L., Yang, D.B., Yu, Y., Wang, W. & Zhao, Q.G. (2011). Geochronology and
777 geochemistry of Mesozoic mafic-ultramafic complexes in the southern Liaoning and
778 southern Jilin province, NE China: Constraints on the spatial extent of destruction of the
779 North China Craton. *Journal of Asian Earth Sciences*, 40, 636–650.
780 Peng, Y.J., Qi, C.D., Zhou, X.D., Lu, X.B., Dong, H.C. & Li, Z. (2012). Transition from Paleo-
781 Asian Ocean domain to circum-Pacific Ocean domain for the Ji-Hei composite orogenic
782 belt (in Chinese with English abstract). *Geology and resources*, 21 (3), 261–265.

783 Petford, N. & Atherton, M. (1996). Na-rich partial melts from newly underplated basaltic crust:
784 the Cordillera Blanca Batholith, Peru. *Journal of Petrology*. 37, 1491–1521.
785 Pitcher, W.S. (1993). The nature and origin of Granite. *Blackie Academic and Professional*. pp.
786 321.
787 Plank, T. & Langmuir, C. H. (1988). An evaluation of the global variations in the major element
788 chemistry of arc basalts. *Earth and Planetary Science Letters*, 90, 349–370.
789 Plank, T. (2005). Constraints from thorium/lanthanum on sediment recycling at subduction zones
790 and the evolution of the continents. *Journal of Petrology*, 46, 921 – 944.
791 Qian, C., Chen, H.J., Lu, L., Pang, X.J., Qin, T. & Wang, Y. (2018). The discovery of
792 Neoarchean granite in Longjiang area, Heilongjiang province. *Acta Geoscientica Sinica*, 39
793 (1), 27 – 36 (in Chinese with English abstract).
794 Reubi, O. & Blundy, J. (2009). A dearth of intermediate melts at subduction zone volcanoes and
795 the petrogenesis of arc andesites. *Nature*, 461, 1269–1273.
796 Rowe, M.C., Wolff, J.A., Gardner, J.N., Ramos, F.C., Teasdale, R. & Heikoop, C.E. (2007).
797 Development of continental volcanic field: Petrogenesis of pre-caldera Intermediate and
798 silicic rocks and origin of Bandelier magmas, Jemez Mountains (New Mexico, USA).
799 *Journal of Petrology*, 48 (11), 2063 –2091.
800 Rubatto, D. (2002). Zircon trace element geochemistry: partitioning with garnet and the link
801 between U–Pb ages and metamorphism. *Chemical Geology*, 184, 123 – 138.
802 Rudnick, R.L., Gao, S., Ling, W.L., Liu, Y.S. & Mc Donough, W.F. (2004). Petrology and
803 geochemistry of spinel peridotite xenoliths from Hannuoba and Qixia, North China Craton.
804 *Lithos*, 77, 609–637.

805 Safonova, I.Y. & Santosh, M. (2014). Accretionary complexes in the Asia-Pacific region: tracing
806 archives of ocean plate stratigraphy and tracking mantle plumes. *Gondwana Research*, 25
807 (1), 126–158.
808 Sengör, A.M.C., Natal'in, B.A. & Burtman, V.S. (1993). Evolution of the Altaid tectonic collage
809 and Paleozoic crustal growth in Eurasia. *Nature*, 364, 299 – 307.
810 Shi, Y., Liu, Z.H., Liu, Y.J., Shi, S.S., Wei, S.S., Yang, J.J. & Gao, T. (2019). Late Paleozoic-
811 Early Mesozoic southward subduction-closure of the Paleo-Asian Ocean: Proof from
812 geochemistry and geochronology of Early Permian-Late Triassic felsic intrusive rocks from
813 North Liaoning, NE China. *Lithos*, 346-347, Doi.org/10.1016j.lithos.2019.105165.
814 Sun, C.Y., Long, X.Y., Xu, W.L., Wang, F., Ge, W.C., Guo, P. & Liu, X.Y. (2018). Zircon U-Pb
815 ages and Hf isotopic compositions of the Heilongjiang Complex from Jiayin, Heilongjiang
816 province and Kundur, Russian Far East and their geological implications. *Acta Petrologica*
817 *Sinica*, 34 (10): 2901–2916.
818 Sun, M. D., Xu, Y. G., Wilde, S. A. & Chen, H. L. (2015). Provenance of Cretaceous trench
819 slope sediments from the Mesozoic Wandashan Orogen, NE China: Implications for
820 determining ancient drainage systems and tectonics of the Paleo-Pacific. *Tectonics*, 34,
821 1269–1289.
822 Sun, S.S. & McDonough, W.F. (1989). Chemical and isotopic systematics of oceanic basalts:
823 implications for mantle composition and processes. In: Saunders, A. D. and Norry, M. J.,
824 eds., Magmatism in ocean basins: *Geological Society*, London, Special Publications 42, no.
825 1, pp. 313–345.
826 Tang, J., Xu, W.L., Wang, F., Wang, W., Xu, M.J. & Zhang, Y.H. (2013). Geochronology and
827 geochemistry of Neoproterozoic magmatism in the Erguna Massif, NE China: petrogenesis

828 and implications for the breakup of the Rodinia supercontinent. *Precambrian Research*, 224,
829 597 – 611.
830 Tang, J., Xu, W.L., Niu, Y.L., Wang, F., Ge, W.C., Sorokin, A.A. & Chekryzhov, I.Y. (2016).
831 Geochronology and geochemistry of Late Cretaceous-Paleocene granitoids in the Sikhote-
832 Alin Orogenic Belt: Petrologenesis and implications for the oblique subduction of the paleo-
833 Pacific plate. *Lithos*, 266-267, 202 – 212.
834 Tamura, A., Ishizuka, O., Stern, R.J., Shukuno, H., Kawabata, H., Embley, R.W., Hirahara, Y.,
835 Chang, Q., Kimura, J.I., Tatsumi, Y., Nunokawa, A. & Bloomer, S.H. (2011). Two primary
836 basalt magma types from Northwest Rota-1 Volcano, Mariana arc and its mantle diaper or
837 mantle wedge plume. *Journal of Petrology* 0, 1 – 41.
838 Tchameni, R., Mezger, K., Nsifa, N.E. & Pouclet, A. (2001). Crustal origin of early Proterozoic
839 syenites in the Congo Craton (Ntem Complex), South Cameroon. *Lithos*, 57, 23 – 42.
840 Turner, S., Arnaud, N., Liu, J., Rogers, N., Hawkesworth, C., Harris, N., Kelley, S., Van
841 Calsteren, P. & Deng, W. (1996). Post-collision, shoshonitic volcanism on the Tibetan
842 Plateau: implications for convective thinning of the lithosphere and the source of ocean
843 island basalts. *Journal of Petrology*, 37, 45–71.
844 Vernikovsky, V.A., Pease, V.L., Vernikovskaya, A.E., Romanov, A.P., Gee, D.G. & Travin,
845 A.V. (2003). First report of early Triassic A-type granite and syenite intrusions from Taimyr:
846 product of the northern Eurasian superplume. *Lithos*, 66, 23 – 66.
847 Vernon, R.H. (1984). Micro-granitoid enclaves: globules of hybrid magma quenched in a
848 plutonic environment. *Nature*, 304, 438 – 439.
849 Wang, F., Xu, W.L., Li, J., Pei, F.P. & Cao, H.H. (2009). Chronology and geochemistry of Early
850 Cretaceous gabbro-diorite in Yantongshan area of Jilin. *Global Geology*, 28 (4), 403–413.

851 Wang, F., Xu, W.L., Xu, Y.G., Gao, F.H. & Ge, W.C. (2015). Late Triassic bimodal igeous
852 rocks in the eastern Heilongjiang province, NE China: Implications for the initiation
853 subduction of the Paleo-pacific plate beneath Eurasia. *Journal of Asian Earth Sciences*, 97,
854 406 – 423.
855 Wang, F., Xu, Y. G., Xu, W. L., Yang, L., Wu, W., & Sun, C. Y. (2017). Early Jurassic calc-
856 alkaline magmatism in Northeast China: Magmatic response to subduction of the Paleo-
857 Pacific plate beneath the Eurasian continent. *Journal of Asian Earth Sciences*, 143, 249–268.
858 Wang, F., Xu, W.L., Xing, K.C., Wang, Y.N., Zhang, H.H., Wu, W., Sun, C.Y. & Ge, W.C.
859 (2019). Final closure of the Paleo-Asian Ocean and onset of subduction of Paleo-Pacific
860 Ocean: Constraints from Early Mesozoic magmatism in the central southern Jilin province,
861 NE China. *Journal of Geophysical Research: Solid Earth*, 124, 2601-2622.
862 Wang, Q., Li, J.W., Jian, P., Zhao, Z.H., Xiong, X.L., Bao, Z.W., Xu, J.F., Li, C.F., Ma, J.L.
863 (2005). Alkaline syenites in eastern Cathaysia (South China): Link to Permian-Triassic
864 transtension. *Earth and Planetary Science Letters*, 230, 339 – 354.
865 Whalen, J.B., Currie, K.L. & Chappell, B.W. (1987). A-type granites: geochemical
866 characteristics, discrimination and petrogenesis. *Contributions to Mineralogy and Petrology*,
867 95, 407 – 419.
868 Wilke, M. & Behrens, H. (1999). The dependence of the partitioning of iron and europium
869 between plagioclase and hydrous tonalitic melt on oxygen fugacity. *Contributions to*
870 *Mineralogy and Petrology*, 137, 102–114.
871 Wu, F.Y., Sun, D.Y., Li, H., Jahn, B.M. & Wilde, S. (2002). A-type granites in northeastern
872 China: age and geochemical constraints on their petrogenesis. *Chemical Geology*, 187 (1),
873 143–173.

874 Wu, F.Y., Yang, J.H., Wilde, S.A. & Zhang, X.O. (2005). Geochronology, petrogenesis and
875 tectonic implications of Jurassic granites in the Liaodong Peninsula, NE China. *Chemical*
876 *Geology*, 221, 127–156.
877 Wu, F.Y., Sun, D.Y., Ge, W.C., Zhang, Y.B., Grant, M.L., Wilde, S.A. & Jahn, B.M. (2011).
878 Geochronology of the Phanerozoic granitoids in northeastern China. *Journal of Asian Earth*
879 *Sciences*, 41, 1 – 30.
880 Xiao, W.J., Windley, B.F., Hao, J. & Zhai, M.G. (2003). Accretion leading to collision and the
881 Permian Solonker suture, Inner Mongolia, China: termination of the Central Asian Orogenic
882 Belt. *Tectonics*, 22,1069 – 1089.
883 Xiao, W.J., Zhang, L.C., Qin, K.Z., Sun, S. & Li, J.Y. (2004). Paleozoic accretionary and
884 collisional tectonics of the eastern Tienshan (China): implications for the continental growth
885 of Central Asia. *American Journal Sciences*, 304, 370–395.
886 Xiao, W.J., Windley, B.F., Sun, S., Li, J.L., Huang, B.C., Han, C.M., Yuan, C., Sun, M. & Chen,
887 H.L. (2015). A tale of amalgamation of three Permo-Triassic collage systems in Central
888 Asia: oroclines, sutures, and terminal accretion. *Annual Review of Earth and Planetary*
889 *Sciences*, 43, 477 – 507.
890 Xu, J.F., Shinjo, R., Defant, M.J., Wang, Q. & Rapp, R.P. (2002). Origin of Mesozoic adakitic
891 intrusive rocks in the Ningzhen area of east China: partial melting of delaminated lower
892 continental crust? *Geology*, 30, 1111–1114.
893 Xu, W.L., Gao, S., Wang, Q.H., Wang, D.Y. & Liu, Y.S. (2006). Mesozoic crustal thickening of
894 the eastern North China Craton: Evidence from eclogite xenoliths and petrologic
895 implications. *Geology*, 34, 721–724.

Xu, W.L., Pei, F.P., Gao, F.H., Yang, D.B. & Bu, Y.J. (2008). Zircon U-Pb age from Basement Granites in Yishu graben and its tectonic implications. *Earth Science*, 33 (2), 145–150 (in Chinese with English abstract).

Xu, W.L., Ji, W.Q., Pei, F.P., Meng, E., Yu, Y., Yang, D.B. & Zhang, X.Z. (2009), Triassic volcanism in eastern Heilongjiang and Jilin Provinces, NE China: Chronology, geochemistry, and tectonic implications. *Journal of Asian Earth Sciences*, 34, 392 – 402.

Xu, W.L., Pei, F.P., Wang, F., Meng, E., Ji, W.Q., Yang, D.B. & Wang, W. (2013). Spatial-temporal relationships of Mesozoic volcanic rocks in NE China: constraints on tectonic overprinting and transformations between multiple tectonic systems. *Journal of Asian Earth Sciences*, 74, 167 – 193.

Xu, W.L., Sun, C.Y., Tang, J., Luan, J.P. & Wang, F. (2019). Basement nature and tectonic evolution of Xing'an-Mongolian Orogenic Belt. *Earth Science*, 44 (5), 1620 – 1646 (in Chinese with English abstract).

Xu, X.S., Dong, C.W., Li, W.X. & Zhou, X.M. (1999). Late Mesozoic intrusive complexes in the coastal area of Fujian SE China: Significance of the gabbro-diorite-granite association. *Lithos*, 46, 299 – 315.

Yang, H., Ge, W.C., Bi, J.H., Wang, Z.H., Tian, D.X., Dong, Y. & Chen, H.J. (2018). The Neoproterozoic-early Paleozoic evolution of the Jiamusi Block, NE China and its east Gondwana connection: Geochenmical and zircon U–Pb–Hf isotopic constraints from the Mashan Complex. *Gondwana Research*, 54, 102 – 121.

Yang, H., Ge, W.C., Zhao, G.C., Bi, J.H., Wang, Z.H., Dong, Y. & Xu, W.L. (2017). Zircon U–Pb ages and geochemistry of newly discovered Neoproterozoic orthogneisses in the Mishan

region, NE China: Constraints on the high–grade metamorphism and tectonic affinity of the Jiamusi-Khanka Block. *Lithos*, 268–271, 16 – 31.

Yang, J.H., Wu, F.Y., Shao, J.A., Wilde, S.A., Xie, L.W. & Liu, X.M. (2006). Constraints on the timing of uplift of the Yanshan Fold and Thrust Belt, North China. *Earth Planetary Science Letters*, 246, 336–352.

Yang, J. H., Sun, J. F., Zhang, M., Wu, F. Y., & Wilde, S. A. (2012). Petrogenesis of silica-saturated and silica-undersaturated syenites in the northern North China craton related to post-collisional and intraplate extension. *Chemical Geology*, 328, 149 – 167.

Ye, H.W. & Zhang, X. (1994). The ^{40}Ar–^{39}Ar age of the vein crossite in blueschist in Mudanjiang area, NE China and its geological implication. *Journal of Changchun University of Earth Sciences*, 24, 369 – 372 (in Chinese with English abstract).

Yu, J.J., Wang, F., Xu, W.L., Gao, F.H. & Tang, J. (2013). Late Permian tectonic evolution at the southeastern margin of the Songnen-Zhangguangcai Range Massif, NE China: Constraints from geochronology and geochemistry of granitoids. *Gondwana Research*, 24, 635–647.

Yu, J. J., Wang, F., Xu, W. L., Gao, F. H., & Pei, F. P. (2012). Early Jurassic mafic magmatism in the Lesser Xing'an ‐ Zhangguangcai Range, NE China, and its tectonic implications: Constraints from zircon U-Pb chronology and geochemistry. *Lithos*, 142–143, 256–266.

Yuan, H.L., Gao, S., Liu, X.M., Li, H.M., Günther, D. & Wu, F.Z. (2004). Accurate U–Pb age and trace element determinations of zircon by laser ablation inductively coupled plasma mass spectrometry. *Geostandard Newsletter*, 28, 353 – 370.

Zhang, C., Wu, X.W., Liu, Z.H., Zhang, Y.J., Guo, W. & Quan, J.Y. (2018). Precambrian geolohical events on the western margin of Songnen Massif: Evience from LA-ICP-MS U-

941 Pb Geochronology of Zircons from Paleoproterozoic granite in the Longjiang Area. *Acta*
942 *Petrologica Sinica*, 34 (10), 3137 – 3152 (in Chinese with English abstract).
943 Zhang, H.H., Wang, F., Xu, W.L., Cao, H.H. & Pei, F.P. (2016). Petrogenesis of Early-Middle
944 Jurassic intrusive rocks in northern Liaoniang and Central Jilin provinces, northeast China:
945 Implications for the extent of spatial-temporal overprinting of the Mongol-Okhotsk and
946 Paleo-Pacific tectonic regimes. *Lithos*, 256-257, 132–147.
947 Zhang, Y.B., Wu, F.Y., Li, H.M., Lu, X.P., Sun, D.Y. & Zhou, H.Y. (2002). Single grain zircon
948 U-Pb ages of Huangniling granite in the Jilin province. *Acta Petrologica Sinica*, 18 (4):
949 475–481 (in Chinese with English abstract).
950 Zhang, Y.B., Wu, F.Y., Wilde, S.A., Zhai, M.G., Lu, X.P. & Sun, D.Y. (2004). Zircon U–Pb
951 ages and tectonic implications of ‘‘Early Paleozoic’’ granitoids at Yanbian, Jilin Province,
952 NE China. *The Island Arc*, 13, 484–505.
953 Zhao, S., Xu, W.L., Tang, J., Li, Y. & Guo, P. (2016). Timing of formation and tectonic nature
954 of the purportedly Neoproterozoic Jiageda Formation of the Erguna Massif, NE China:
955 Constraints from field geology and U-Pb geochronology of detrital and magmatic zircons.
956 *Precambrian Research*, 281, 585 – 601.
957 Zheng, C.Z., Wang, G.Q., Yang, S.Y. & Peng, Y.J. (1999). Discovery of Late Carboniferous
958 Weining age fauna from Shitoukoumen Faulted through basin in Jilin and its implication.
959 *Geological Review*, 45 (6), 632–639 (in Chinese with English abstract).
960 Zhou, J. B., Wilde, S. A., Zhang, X. Z., Zhao, G. C., Zheng, C. Q., Wang, Y. J. & Zhang, X. H.
961 (2009). The onset of Pacific margin accretion in NE China: Evidence from the Heilongjiang
962 high pressure metamorphic belt. *Tectonophysics*, 478, 230–246.

963 Zhou, J.B. & Li, L. (2017a). The Mesozoic accretionary complex in Northeast China: Evidence
964 for the accretion history of Paleo-Pacific subduction. *Journal of Asian Earth Sciences*, 145,
965 91–100.
966 Zhou, J.B., Wilde, S..A., Zhao, G.C. & Han, J. (2018). Nature and assembly of microcontinental
967 blocks within the Paleo-Asian Ocean. *Earth Science Reviews*, 186, 76–93.
968 Zhou, X.D., Sun, C.L. & Peng, Y.J. (2009). Reference sections of Carboniferous and Permian
969 boundary in Xing'an-Mongolia and Jilin-Heilongjiang Orogenic Belt. *Journal of Jilin*
970 *University (Earth Science Edition)*, 39 (1), 72–79 (in Chinese with English abstract).
971 Zhou, Z.B., Pei, F.P., Wang, Z.W., Cao, H.H., Xu, W.L., Wang, Z.J. & Zhang, Y. (2017b).
972 Using detrital zircons from late Permian to Triassic sedimentary rocks in the south-eastern
973 Central Asian Orogenic Belt (NE China) to constrain the timing of final closure of the
974 Paleo-Asain Ocean. *Journal Asian Earth Sciences*, 144, 82 – 109.